Investigating Specimen Preparation and Characterization Methods of Semiconductor Material

Jamie Carol Roberts
B.A. Political Science- International Relations, University of Wisconsin- Madison, 2005
B.S. Physics, University of Missouri- St. Louis, 2014

A Thesis Submitted to The Graduate School at the University of Missouri-St. Louis in partial fulfillment of the requirements for the degree
Master of Science in Physics with an emphasis in Applied Physics

December 2016

Advisory Committee

Phillip Fraundorf, Ph.D.
Chairperson

David Osborn, Ph.D.

Bernard Feldman, Ph.D.

Abstract

The ability to prepare and characterize semiconductor material has wide implications for research to improve solar cell and device efficiencies. The variety of preparation techniques and characterization methods available allow us to explore materials in ways that were once not possible. However, the ability to obtain statistical information from prepared specimens is limited by residue caused by the specimen preparation process, the amount of volume or surface area that can be made accessible to characterization techniques, and the need for human pattern recognition to identify each structure, often given information on data obtained at more than one specimen orientation. This project explores some of those limitations through specimen preparation methods and characterization techniques. The research shows epitaxial lift-off in GaSb thin films is possible, that red, green and blue (RGB) pixel values can be used to measure thickness (within certain limitations including specimen image grey value and ambient lighting), and that oxygen cluster nucleation has a thermal history dependence that contributes to differences in oxygen precipitation (which correlates to functionality differences in device properties). These results contribute to advancements for semiconductor research and allow material advancements for more efficient solar and device performance in the future.

Table of Contents

1 Introduction

The ability to prepare and characterize semiconductor materials has wide implications for research to improve solar cell and device efficiencies. Tools like transmission electron microscopes (TEM) allow us to record the result of a myriad of electron scattering experiments on individual submicron defects in crystals. However, the ability to obtain statistical information from a population of such defects is limited by residue caused by the specimen preparation process, the amount of volume that can be made accessible to strongly interacting electrons, and the need for human pattern recognition to identify each structure, often given information on data obtained at more than one specimen orientation. This project will explore some of the limitations.

In chapter 2, epitaxial lift-off (ELO) is demonstrated and improved for thin film GaSb specimens. Advancing our scientific knowledge in the field of III-V photovoltaics now will help us make greater strides toward implementing it commercially in the future. By utilizing layers of thin film GaAs and GaSb in a multilayer solar cell, less material will be needed, and thus costs will be lowered. In addition, this type of multilayer junction will hypothetically capture a larger range of photonic energy, increasing the efficiency of solar cells. Photolithography and focused ion beam specimen preparation techniques are also discussed as background material in this chapter.

Thickness measurements of prepared samples and metrology on the TEM is considered in chapter 3, with a focus on the RGB method. Since wide focal depth of electron microscopes makes TEM data inherently two dimensional, retrieving information on the thickness of specimens can be difficult. However, silicon exhibits a characteristic color change with respect to the material's thickness that can be utilized as a thickness characterization method. Since color images with red, green and blue (RGB) pixel values are now widely available and more mobile than ever, this method of thickness calibration can become a valuable tool with the ability to both record RGB values and transmit the data across the globe in seconds. Quantitative use of these RGB values, however, is in its infancy. Oxygen-rich silicon specimens contain stacking fault defects may provide a geometrical tool for measuring the specimen thickness at a given point, and can be used to further the study of the RGB method. Through these quantitative applications, measuring the thickness of semiconductor silicon specimens that have been thinned for examination in a transmission electron microscope are investigated in the chapter.

In chapter 4, oxygen related defects in semiconductor silicon is explored. Nucleation theory is predicated on the evolution of a "pre-critical cluster distribution", something that in gas and liquid phase nucleation and growth studies is difficult to approach experimentally, except, perhaps, statistically via a scattering technique. In solid-state nucleation and growth settings, however, the "quench," or fast cooling, often allows one to freeze the distributions in place for a cluster-by-cluster look. Chapter 4 will examine this issue with the interesting case of

Czochralski (Cz) semiconductor-silicon. [1] Oxygen from the growth crucible, uninvited but unavoidable, has proven to be a possible ally to the device manufacturing process by strengthening the wafer and by precipitating to create defects capable of trapping electrically active impurities, thus improving device yields. Therefore, there is a practical interest in controlling the oxygen-cluster behavior. The use of annealing, ion milling, and tripod polishing for creating transmission electron microscope (TEM) samples is also discussed as background information to this chapter.

The final chapter, chapter 5, is a summary of the results of this body of work. These findings are discussed and possibilities for future work in these areas are considered.

2 Epitaxial Lift-Off

The method of epitaxial lift-off (ELO) involves the removal of a thin epitaxial film from a host substrate. This technique has been successfully used in GaAs films with Ga substrates, but had not previously been explored for GaSb thin films on any substrates. This chapter will show the methods and results used to successfully utilize this technique and maintain quality thin films for device preparation. Techniques utilized include photolithography and cross-sectional sample preparation utilizing a focused ion beam (FIB) in the scanning electron microscope (SEM) for characterization of the sample in the transmission electron microscope (TEM).

2.1 Epitaxial Lift-Off Background

2.1.1 Photolithography and Diode Fabrication

Photolithography is a process used in the fabrication of semiconductor devices. The process utilizes light-sensitive chemicals called photoresists, UV light, and geometric masks, in conjunction with material deposition methods, to construct the desired device structure. For this project, photolithography was used to fabricate thin film GaSb materials into diodes for further characterization. The GaSb thin films were fabricated by the laboratory manager, with my participation as an observer, utilizing molecular beam epitaxy (MBE). It was also utilized in the etchant investigation discussed in part 2.2.2. Figure 2.1 gives a sample of the masks used to fabricate contacts.

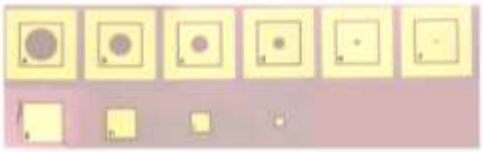

Figure 2.1: Image of masks used. The large square is 300µm.

After GaSb thin films are removed from their substrates, general diode fabrication can take place. This process involved photolithography (applying a photoresist, UV exposure, and development), metallization of the contacts, annealing, and epitaxial lift-off (ELO). Then, a second round of photolithography, including an alignment of the mask with the previous round and dry etching, completed the diode fabrication process. For the thin films, the top contacts were covered with 3µm of copper bonded to a Kapton sheet with black wax. After ELO, the wax was removed and the back contact was deposited on the ELO side of the sample. The Kapton tape, adhered to the copper, was used to hold the sample while metallizing. Next, 100Å of Cr and 600Å of Au were deposited on the Kapton sheet through deposition in the metal evaporator, and the thin diode was bonded to the golden Kapton sheet. Finally, a copper etch took place to complete the process.

The efficiency of the thin film diode was then tested, with results shown below. The results were compared to GaAs diodes, as epitaxial lift-off methods have previously been shown to work in literature. [6] Choosing a specific mask for use in fabricating the diode was also investigated, using mask area to diode curve graphs. For determining which mask ought to be utilized, GaAs was utilized as the test material.

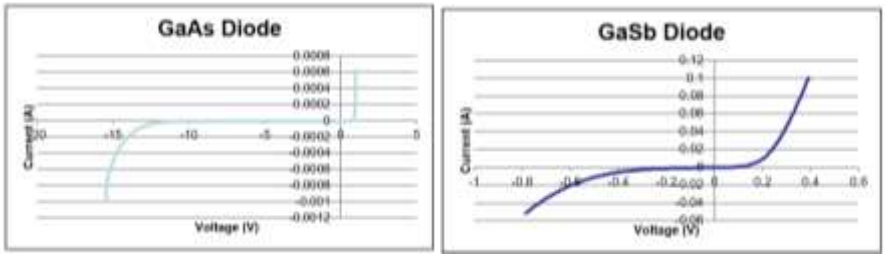

Figure 2.2: I-V Measurements of GaAs and GaSb Thin-Film Diodes

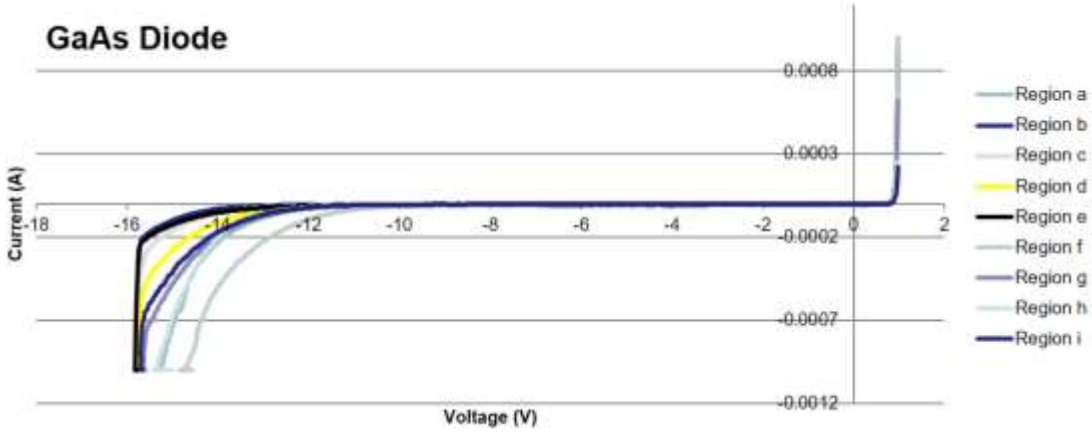

Figure 2.3: Diode Characteristics by Mask Area. Mask area labels from figure 2.1.

2.1.2 Focused Ion Beam

The Focused Ion Beam (FIB) is a specimen preparation technique, most popular in the semiconductor and material science industries. It can be used for deposition or removal of material in a small, micron-sized area. The FIB equipment utilized for this project was integrated into an SEM apparatus and used simultaneously. This means that the specimen on which the FIB will be utilized must conform to SEM sample preparation. Thus, the specimen must be dry, conductive or possess an applied conductive coating, small enough to fit in the holder, and thin- though not nearly as thin as a TEM sample.

The FIB was utilized in experimentation for this project as a tool to cut a cross-sectional TEM sample of a GaSb film that had gone through the ELO process. The purpose was to investigate the thickness of the oxidation layer. Below are SEM images of the process and TEM images of the results.

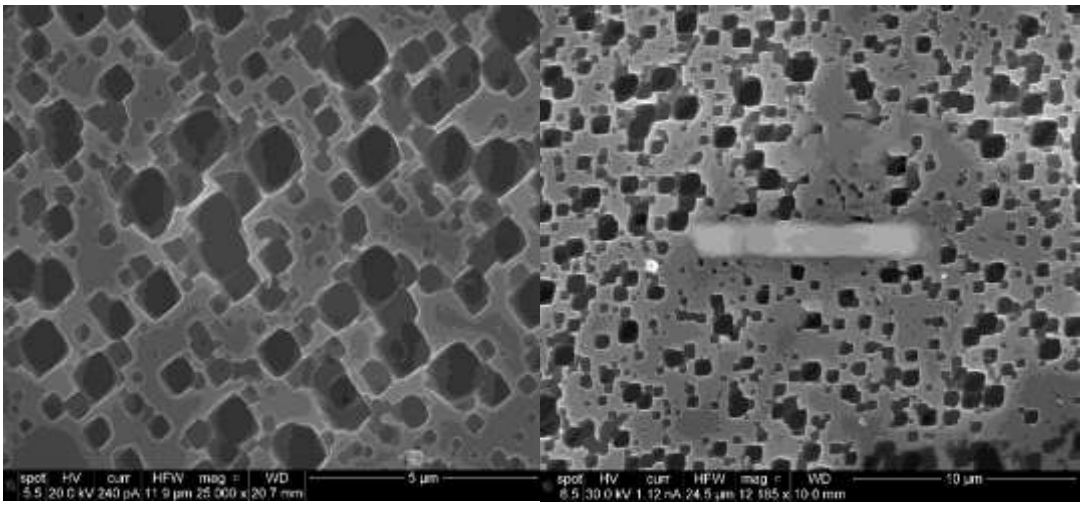

Figure 2.4: SEM images before and after FIB cross-sectional cut

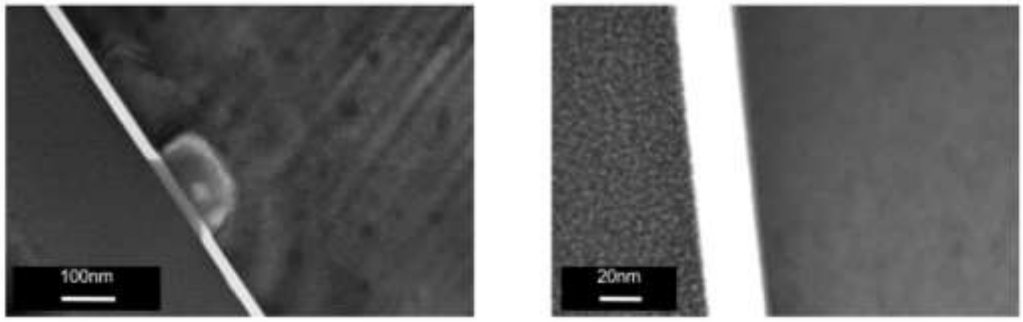

Figure 2.5: TEM image of cross-sectional sample

2.2 Epitaxial Lift-Off Methods

2.2.1 Substrate Removal Versus Epitaxial Lift-Off

Epitaxial layers, which make up the device, can be isolated from the substrate by different techniques. Two of the most common techniques are substrate removal

and epitaxial lift-off (ELO). On the substrate removal technique, an etch stop layer is grown between the device and the substrate to protect the device while the substrate is completely etched away. After the substrate is removed then the etch stop layer is also removed, via a separate etching process. To successfully isolate the device, the etchants used must have a high selectivity for the materials being etched. With the ELO method, the structure does not have an etch stop layer between the device and the substrate, it has a sacrificial layer that can be laterally etched away with a highly selective etchant, leaving both the epilayer and the substrate intact. These techniques have been extensively investigated for GaAs, InAs and InP systems but not for antimonide systems. The techniques are illustrated in figure 2.6.

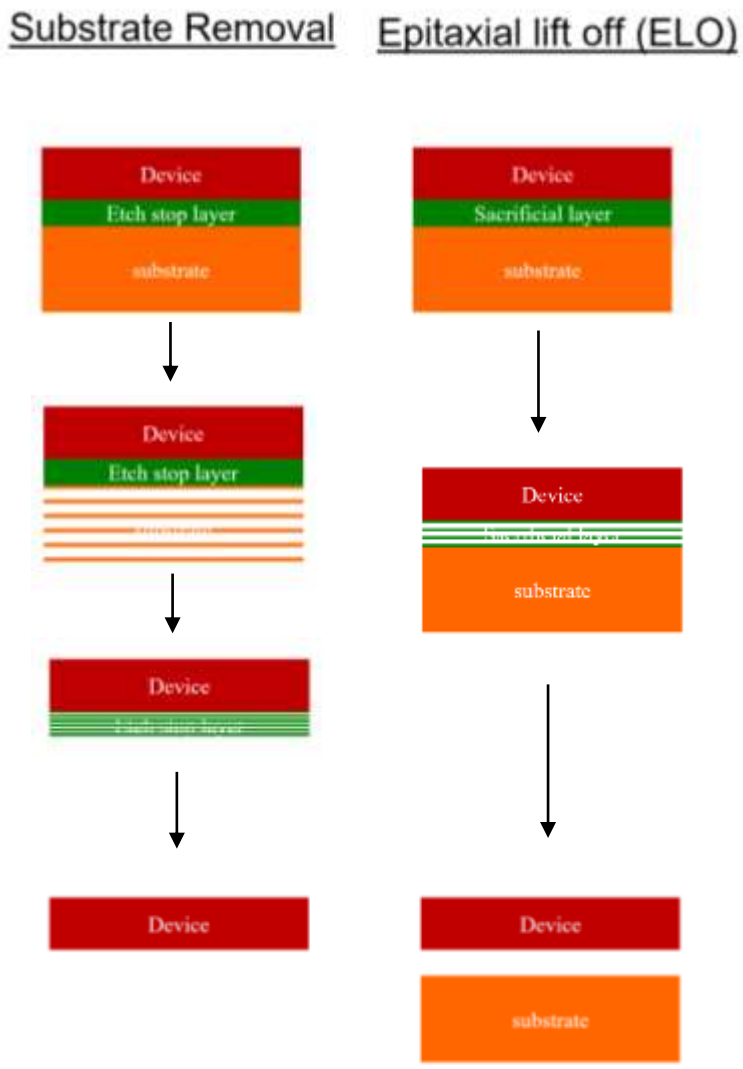

Figure 2.6: Substrate Removal versus Epitaxial Lift-Off Process

Since ELO is a process that enables the separation of the epilayer from the original substrate without damaging the substrate, it brings many advantages. The ability to isolate the device from the substrate reduces the device weight. It increases its flexibility and reduces heat resistance. It also shows increased optical efficiency and allows for easier integration with other materials. In addition, since the substrate

remains intact, it can be reused, and hence significantly decreases the cost of devices.

The isolation of thin GaSb films could have a significant impact in the middle to long wave infrared optoelectronic devices. For example, high power lasers require substrates with high thermal conductivity, as heat dissipation is crucial for their performance. Focal plane arrays require substrates with low absorption. Therefore, the possibility of transferring these devices to more appropriate substrates could significantly improve their performance.

Previously, the challenges of isolating GaSb devices were examined, and ELO was not a favorable method due to a lack of highly selective etchants. [5] The solution to this issue is to grow the GaSb devices on a GaAs substrate, and then use the typical ELO methods described in literature. [6][7][8]

The physical separation of GaAs epilayers from their GaAs substrate was first reported by Konagai et al. in 1978, with the motivation being a reduction in the cost of GaAs cells. [6] Epitaxial films of GaAs with a 30 micron thickness were grown on a GaAs substrate with a sacrificial etch layer of AlGaAs (70% aluminum) between the substrate and the GaAs epilayer. After processing the top metal contacts, the surface was protected with a black wax coating and the sample immersed in a HF solution to selectively etch the AlGaAs layer. [6] This was the initial (and at one time, the only) demonstration of epitaxial lift off, but now the

technique has been extensively explored and improved, with the main purpose continuing to be a cost reduction of III-V solar cells.

For this project, three structures, as shown in figure 2.7, were selected and fabricated through MBE for analysis using the ELO technique.

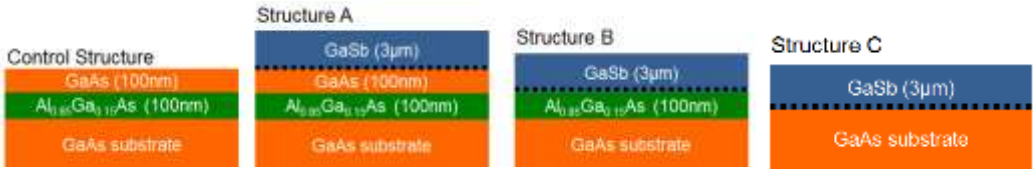

Figure 2.7: Three structures for use in ELO Analysis

On structure A, GaSb was grown on a typical GaAs etch system to explore the possibility of isolating GaSb-based materials by using well established GaAs substrate removal techniques. This could be done either by completely etching the substrate away (substrate removal) or by epitaxial lift off. On Structure B, GaSb was grown directly on the AlGaAs etch stop layer, or the sacrificial layer, allowing for either substrate removal or ELO techniques for isolating the device. On structure C, GaSb is grown directly on a GaAs substrate, where the possibility of etching the substrate is the main goal to be explored. This would be done through investigating the etch contrast between GaSb and GaAs, where interfacial mismatch (IMF) growth should enable the use of ELO for GaSb. The following figures are high resolution TEM images of structures A and B.

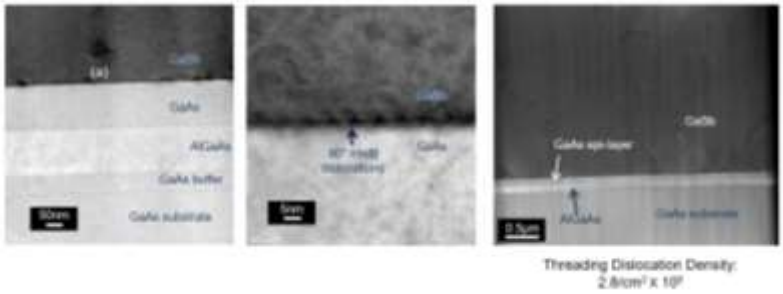

Figure 2.8: Structure A High Resolution TEM images

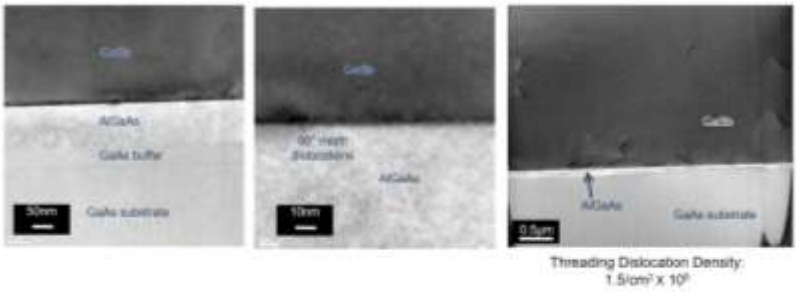

Figure 2.9: Structure B High Resolution TEM images

The growth of GaSb epi-layers with 100 % relaxation and low threading dislocation density has been demonstrated by inducing arrays of 90° IMF dislocations at the GaSb/GaAs interface, despite their 7.78% lattice mismatch. [9] The residual threading dislocation density is in the GaSb layer, and is in the range of 10^7 to 10^8 defects per cm^2. This sufficiently meets the requirements of a wide range of devices.

The initial round of using the basic ELO technique compared with substrate removal showed an advantage with ELO with structure B, and substrate removal with structure A. As seen in figure 2.10 below, an x-ray diffraction (XRD) analysis

of the structures illustrates this comparison. This prompted further study of ELO techniques to work on improving the outcomes for both structures.

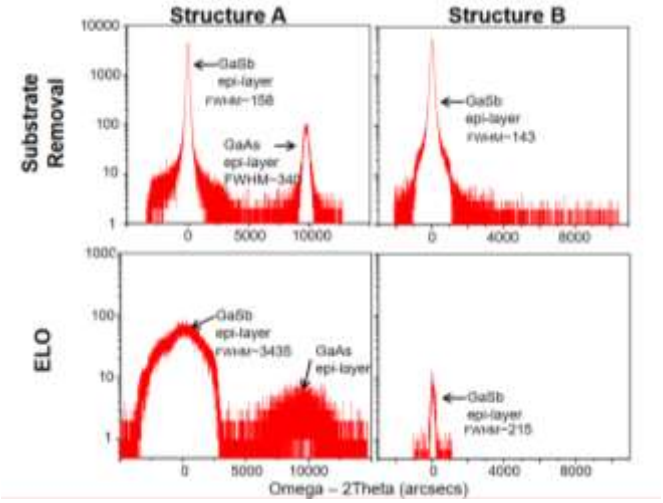

Figure 2.10: Comparing Substrate Removal versus ELO

2.2.2 Investigating Etchant Solutions

Etchant solutions were investigated to determine which would be the most effective at removing the sacrificial layer while leaving the device undamaged. Generally, etchants react with only one material, leaving the other intact. However, HF reacts with both GaAs and GaSB. Thus, the rates of reactions for HF solutions must be inspected. Three HF solutions were chosen: 10% HF, 49% HF, and an HF solution containing a buffer called a buffered oxide etchant, or BOE. To undercut a very thin film over its entire area without affecting the film or the substrate, the selectivity must be extremely high. The isolation of epi-layers from GaSb substrates is a difficult process since the existing wet etchant solutions for antimonide-based materials have very low selectivities, and the thickness of the etch stop layer, InAs,

is restricted by the lattice mismatch between InAs and GaSb. By utilizing a GaAs substrate, this challenge should be mitigated.

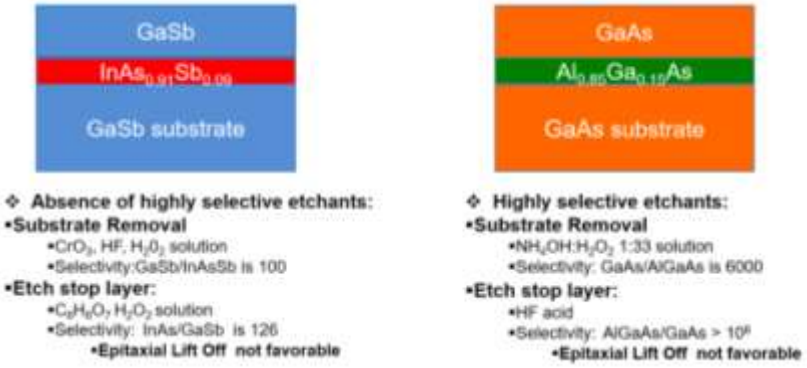

Figure 2.11: Challenge with Isolating GaSb Devices [7] [10] [11]

Six specimens (3 GaSb samples and 3 GaAs samples) were prepared for submersion in the etchant solution. Each specimen was cleaned with acetone, methanol, isopropanol and water, then dried thoroughly. A photoresist was applied and annealed at 200°C, then UV exposed. Then, each of the specimens were placed into a solution for 15 hours.

Initial results, by eye, showed that the BOE and 10% solutions would be the most efficient for this project. Further investigation through Nomarski imaging showed the 10% solution to be the best. An example of one of the structures in an HF etchant solution being investigated is shown in figure 2.12. Figure 2.13 shows the results for all six specimens, utilizing Nomarski surface analysis. This technique is also known as Nomarski microscopy or Nomarski interface contrast, uses polarized light to enhance contrast on otherwise invisible surface defects and contaminants.

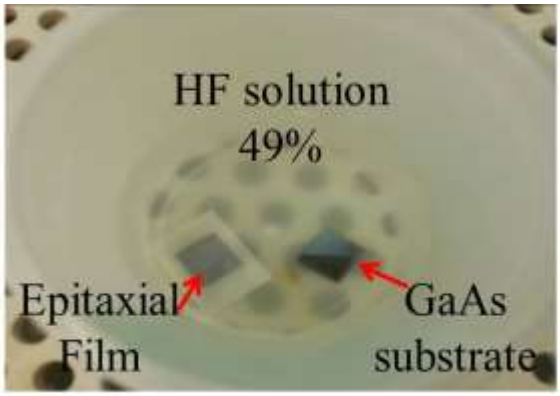

Figure 2.12: HF solution bath for removal of the growth from the substrate

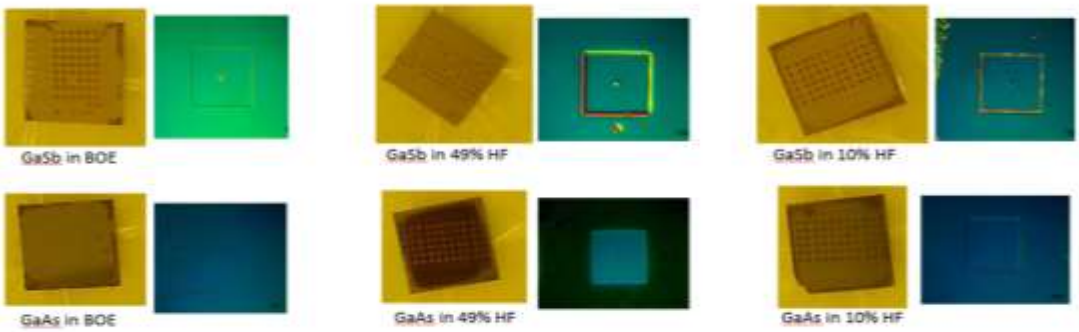

Figure 2.13: Etchant Solution Investigation Results

2.2.3 Investigating ELO Methods

With structures A and B and the control structure, two ELO techniques were investigated: The Yablonovitch Black Wax method and the Schermer Rolling method. Under the black wax method, the layer of wax places the epilayer under tension. This causes the epilayers to slightly curl away from the growth substrate, allowing more etchant to penetrate the sacrificial layer. This will minimize the time needed for the structure to be submerged in the etchant solution, consequently minimizing damage to the device and substrate.

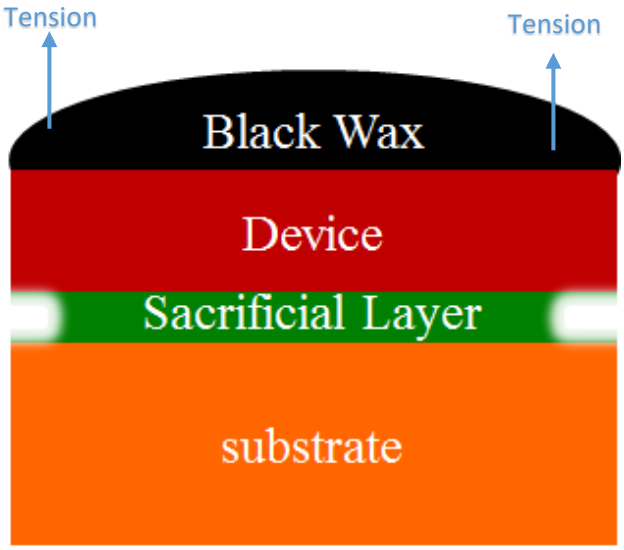

Figure 2.14: Black Wax method, from Yablonovitch

For the Schermer Rolling Method, a cylinder was attached to the device layer, using Kapton tape, and a roller was used to very slowly (over the course of days) peel the device away from the sacrificial layer. Again this allows more etchant to penetrate and remove that layer more quickly, thus minimizing damage to the device and substrate. This method metallizes and mounts samples to a flexible carrier, and uses a cylinder to lift the growth off the substrate after sufficient etching of the sacrificial layer, as shown in the figure below. [8] It has been explored in literature for it's potential to replace the more widely used black wax ELO method, and offers possible solutions to issues encountered from that method.

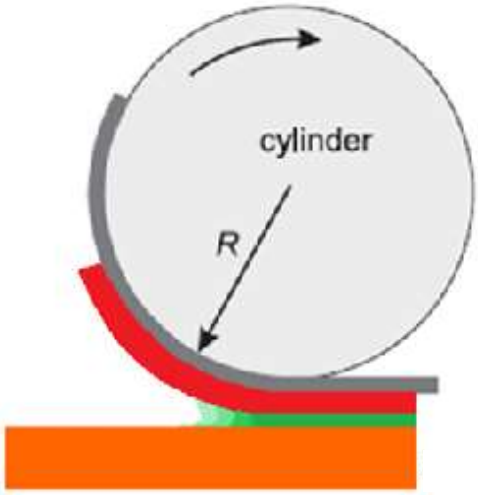

Figure 2.15: Schermer Rolling Method for ELO

Each specimen was prepared for ELO through cleaning (using acetone, methanol, isopropanol and water) and drying. Next, back wax was melted onto Kapton tape at 185^{o}C, and the specimen was placed on top of the wax. Pressure was applied to create a bond, and once cooled, extra black wax was removed with toluene. The results of the specimen trials found that the black wax method was more efficient, and should be used as the chosen method of ELO for this research project, as described below.

After a 10% solution of HF etchant was chosen, the samples were tested for the amount of time needed for effective ELO to take place. The first sample remained in the solution for approximately 52 hours. When removed, separation had begun. Separation of the device was encouraged with the Schermer method. The results include some damage to the thin film, and the substrate remaining intact.

Figure 2.16: Sample 1 Results: Schermer Method

The second sample remained in the acid for 52 hours, with separation being encouraged with the Yablonovitch method. When removed, separation had begun, but was not complete. Further separation was encouraged with tweezers. The results included some damage to the thin film, with the substrate remaining intact.

Figure 2.17: Sample 2 Results: Black Wax Method

The final sample was left in the solution for 73 hours. When removed, no signs of etching were evident from the black wax method. However, when cleaned with Toluene (to remove the wax), the device and substrate easily separated, revealing a clean etch. There was no damage to the substrate or thin film.

Figure 2.18: Sample 3 Results: Black Wax Method

Thus, this part of the process led to the conclusion that ELO was possible for all three structures, and the most minimally invasive technique (Black wax remaining in an etchant for 73 hours) showed evidence of the least damage to the thin film.

2.3 Epitaxial Lift-Off Results

The III-V semiconductor part of this project used material characterizations for photovoltaic applications focused on finding innovative ways to boost solar cell efficiencies and reduce costs. Although silicon is an inexpensive and easily fabricated semiconductor compared to the use of III-V semiconductors, it's efficiency rate leaves much room for improvement. As the demand for energy continues to rise and byproducts from traditional energy sources become larger sources of pollutants and drains on natural resources, the ability to supplement and replace many of our existing power systems with clean, renewable technology is going to become even more important. Gallium antimonide was studied in this project for its potential in creating these necessary advancements in energy technology, and the results are discussed in this section. In order to explore and analyze GaSb for use in multijunction solar cells, the substrate removal technique and epitaxial lift-off (ELO) were investigated, and the crystal and surface quality of the isolated film was characterized.

Fabricating compound III-V semiconductors for use as devices involves the growth of III-V semiconductors on a substrate. To accurately characterize the material

itself, it must be removed from the growth substrate. Though various substrate removal and epitaxial lift-off methods have been shown to work for GaAs, the isolation of thin film GaSb had yet to be successfully reported. This project focused on creating successful epitaxial lift-off (ELO) of GaSb semiconductor thin film structures grown through molecular beam epitaxy (MBE).

There were four key elements to the research plan: investigate the effects of HF on GaSb and GaAs, explore the specific methods of ELO, characterize quality of thin films, and diode fabrication and analysis. After an etchant was chosen and ELO had been achieved, the thin film was characterized for quality. Several methods were employed to analyze the films, including Nomarski microscopy and scanning electron microscopy (SEM). These methods helped categorize defects and determine if the film was sufficient for use in solar cells.

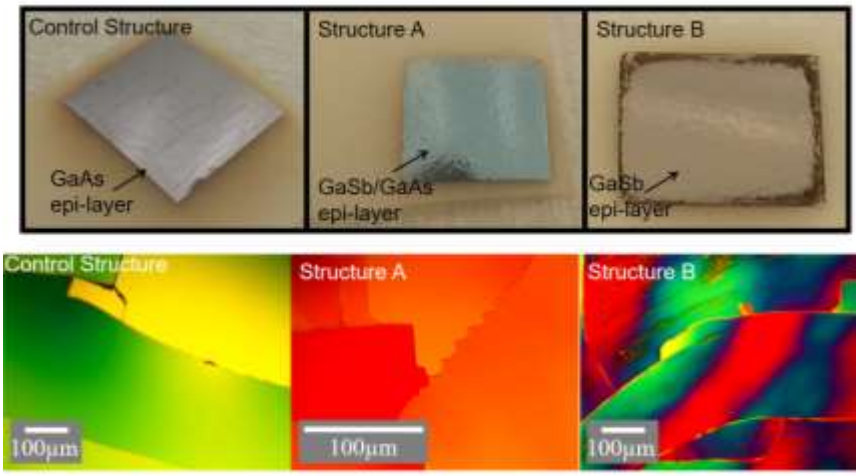

Figure 2.19: ELO Results using Nomarski Analysis. Images of films (upper). Nomarski images for corresponding structure (lower)

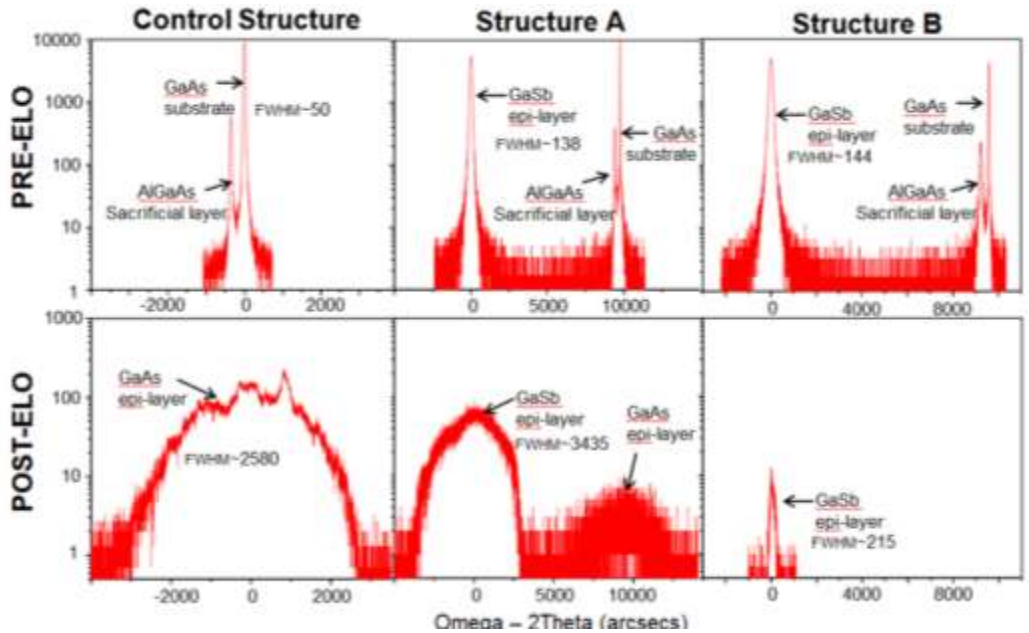

Figure 2.20: ELO Characterization using XRD Analysis for each structure

Two problems encountered with using ELO and 10% etchant solution were the oxidation of the GaSb film and surface damage to the thin film. The solution to this was to use copper as a protective layer against oxidation, and to add another layer of GaAs to protect the thin film surface during etching.

Figure 2.21: Problems with GaSb films- cracking and oxidation

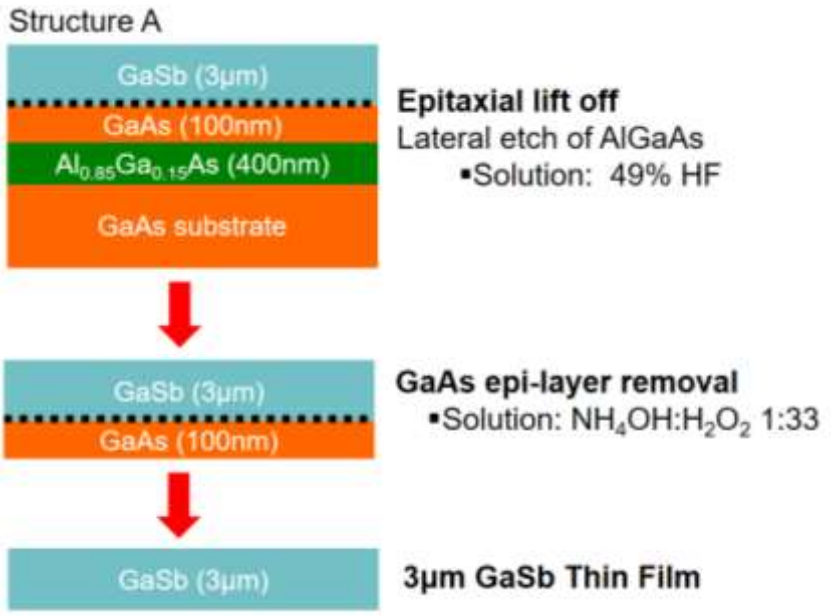

Figure 22: Use of GaAs as a Protective Layer

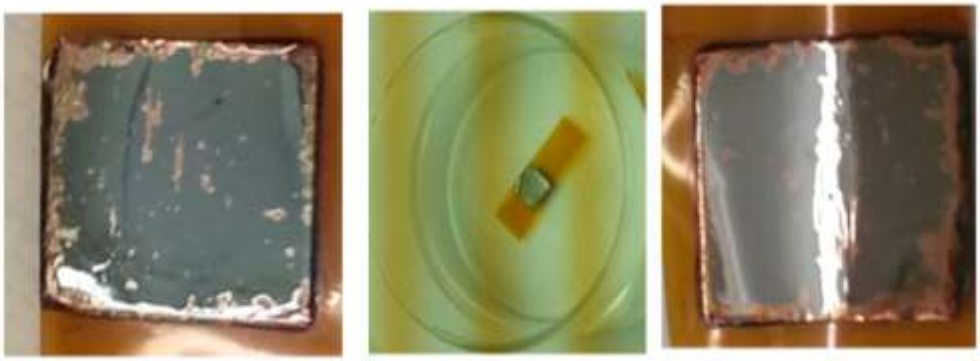

Figure 2.23: Use of copper protection layer

The results of this piece of the project were to conclude that epitaxial lift-off was possible for all three structures, and that adding a layer of GaAs as protection improved surface quality, and adding a layer of copper reduced surface cracking in the thin films.

Figure 2.24: Copper and GaAs protective layers result in better thin films

3 RGB Analysis

Sub-microscopic defects such as oxygen-precipitates, which can act as impurity-getters, play an important role as allies in the semiconductor device manufacturing process. These can only be examined in the TEM after the specimen undergoes a preparation process. However, determining thickness in such specimens can be quite difficult. The standard method used to gain thickness information is identifying thickness fringes through TEM images and analyzing them to determine a thickness value. However, this only works on specimens not beset with bend-contours caused by strain or very thin wedge angles. Thus, RGB analysis was examined for this project, utilizing stacking faults and single crystal thickness fringes as calibration methods. RGB analysis utilizes the differential photon absorption of light transmitted through a specimen to determine the thickness in a given region.

3.1 RGB Analysis Background

3.1.1 Stacking Faults

One method for determining sample thickness in a given region is through the use of stacking fault defects in the material. These “puddles” of silicon self-interstitials, lie on {111} planes in silicon and are bounded by partial dislocations, often large enough to intersect both top and bottom surfaces of the TEM specimen. Since both their orientation and the electron beam’s orientation with respect to the silicon lattice is known, the lateral separation between top and bottom surface-intersections

provides a direct measure of specimen thickness. Figure 3.1 is the TEM image of a specimen, showing both a stacking fault and the edge of the specimen perforation, allowing for both thickness and wedge angle data to be established. Thus once located, these defects can give important information about the thickness of the region they lie in and thus the wedge angle from the perforation. Figure 3.2 shows a stacking fault, whose known habit plane and intersection with the top and bottom surfaces of the thinned silicon specimen allows for rather precise local thickness determination. The field-width of this 300 keV electron image is about 3.98 μm, making the projected breadth of the stacking-fault truncations about 656 nm. Multiplying this by Tan (54.7^{o}) for the angle between {111} and the {100} beam direction gives us a local specimen thickness of about 0.92 μm. Here, the angle (54.7^{o}) is the found the traditional way in which one calculates the angle between two planes, since we have a Cartesian cubic unit cell. It is the dot product of the Miller indices (in our case vector (111) dotted with vector (100)) divided by the magnitude, and set equal to the cosine of the angle.

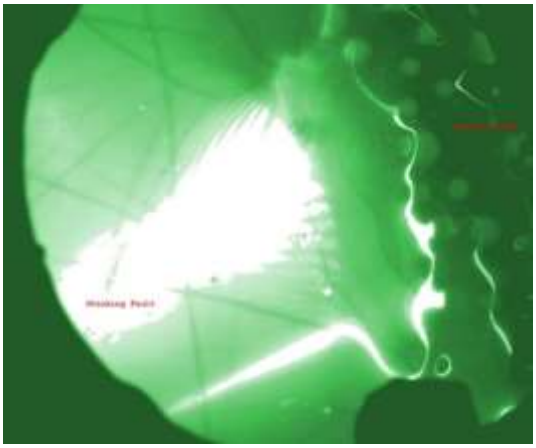

Figure 3.1: Darkfield image of a stacking fault (center left) near the perforation edge (top right).

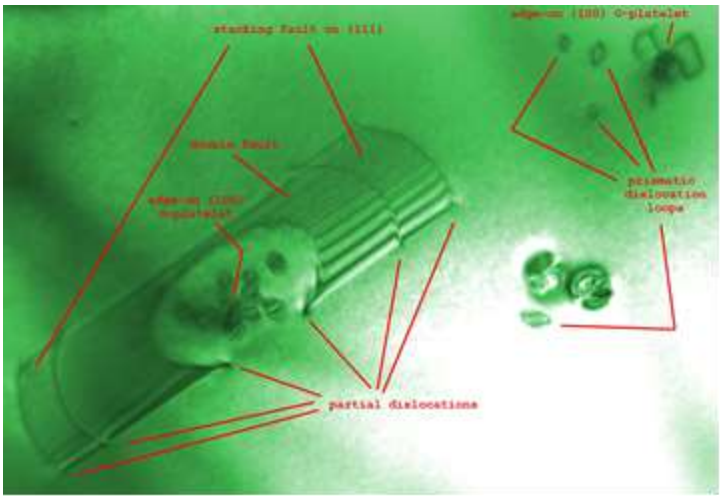

Figure 3.2: Stacking fault associated with late stage oxygen precipitation.

3.2 RGB Analysis Methods

Since many thinned specimens are beset with strain bend-contours or very small wedge angles and may not have stacking faults available for a geometric thickness analysis, another method must be used. Fortunately, semiconductor silicon exhibits useful color changes in transmitted light, from opaque to red to yellow to white, as its thickness decreases below a few microns. This part of the project investigated a new technique to obtain such measurements based on the contrast of visible transmitted color light.

Ordinary color images of a silicon wedge taken with an inexpensive light microscope might therefore supplement data available from the TEM itself. The purpose of this research is to compare this new technique with known methods to determine silicon thickness and wedge-angle. This is completed by comparing RGB

data with thickness fringe data from regions of specimens where both methods may be applied.

To begin the process of obtaining an RGB thickness measurement, a perforated specimen is lighted from beneath, allowing light to shine through the hole and thinner portions of the sample. The sample was placed on a small puncture in dark paper, allowing only light from directly beneath the specimen to come through. Other extraneous light from the room was mitigated to prevent reflected light from around and above the specimen from contaminating the data. Once the effect from external light is negligible and the only transmitted light is coming from beneath the specimen, digital images from a light microscope were recorded.

Figure 3.3: Amscope microscope pictures of perforation of specimens 1-3 (from left to right) for RGB analysis. Perforations on 200-500 micron scale. Blue line marks an example of line length, or "run", as described below.

The images were then used to analyze the wedge angle by finding the thickness of a sample in two places (in the hole, where thickness equals zero, and on the specimen's thin area surrounding the hole), and analyzing that data as the "rise" and "run" of a triangle to obtain the degree of the angle. Using the program Image J, a

pixel both inside (the hole) and "outside" (on the specimen) of the perforation was chosen. The RGB values and x and y coordinates of the pixels were recorded. Using the x and y coordinates obtained from both pixels, the length of the line was calculated using standard vector algebra: $\sqrt{[(X_2-X_{1)}^2 + (Y_2-Y_1)^2]}$. This length was considered the "run" for calculating the angle, and an example is marked in blue on the figure above. The distance in pixels was changed into units of length measurement using the image field width.

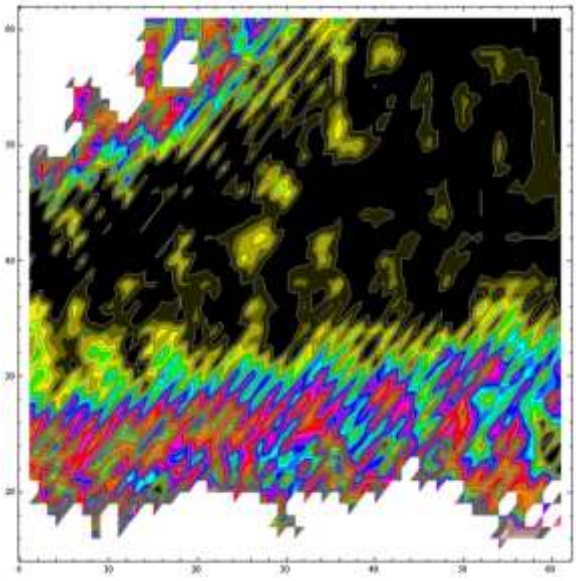

Figure 3.4: Specimen 2 silicon color contour map showing specimen thickness around the hole

To find the "rise," the RGB numbers obtained from each pixel were inserted into the equation $[(G/G_0)/(R/R_0)]$ where G is the green number on the specimen, G_0 is the green measurement in the hole, R is the red number on the specimen, and R_0 is the red measurement in the hole. The results obtained are defined as (G/R), the green to red attenuation. The thickness of the specimen was then acquired from the function $(G/R) \approx 1-0.217t+0.0165t^2$, where t is thickness. This function was

derived from the color of silicon transmission chart, figure 3.5, and is shown graphically on the thickness versus attenuation chart, presented in figure 3.6. [33] For better accuracy, several lines were chosen to measure the variables in each region, and an average of the group was used to calculate the final data. Once the rise and run were found, the equation tanΘ= rise/run was used to compute the wedge angle of the specimen, meaning a right triangle is assumed.

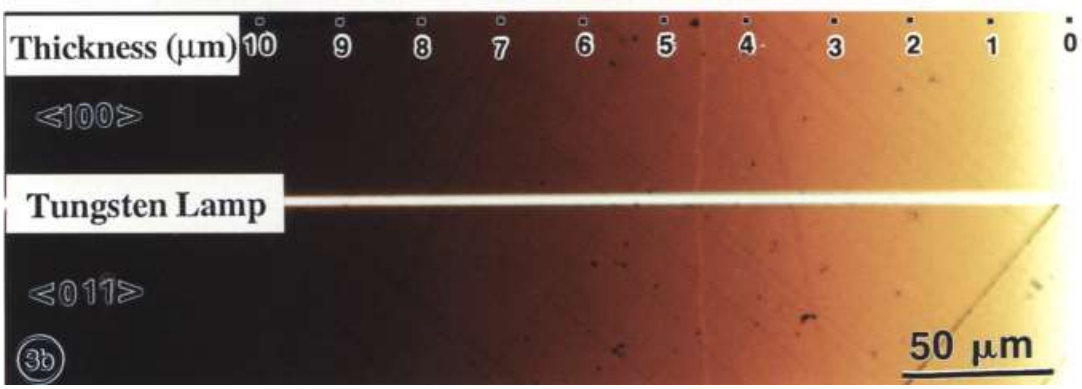

Figure 3.5: Color Transmission Chart from McCaffrey [4]

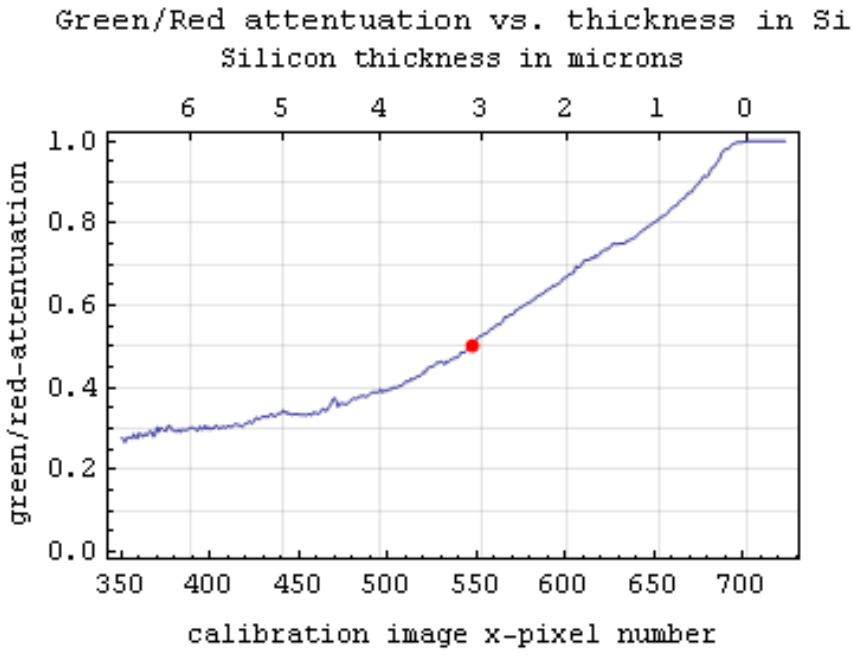

Figure 3.6: Thickness calculation function chart

3.3 RGB Analysis Results

After finding thickness data from RGB analysis, each specimen was examined in the TEM for thickness fringes. A photo of the thickness fringes was taken in the TEM of each wedge angle area on the sample. Using the distance between fringes, information on silicon extinction distances and the spacing orientation of the sample, wedge angles could be calculated by this method to compare to the information taken from RGB analysis. [12]

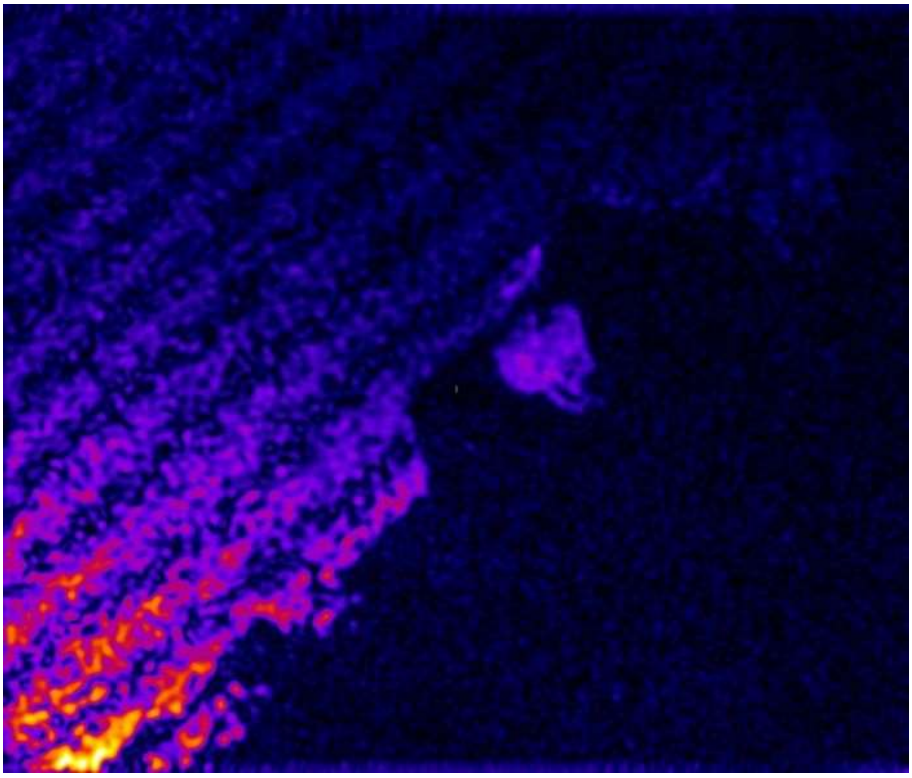

Figure 3.7: TEM thickness fringes from specimen 1

Theoretically, the wedge angles measured by each method for the different areas on each specimen should compare, and the expectation would be a one to one correlation. However, in real data, differences in pixel dpi mean that we are not

actually measuring the same thing, as the scale is quite different- microns versus millimeters. To be theoretically true, we are making the assumption that the different methods will correspond due to the scales used to measure the run in each case. Wedge angles found for each area of each specimen are plotted in figure 3.8. The theory line of a one to one angle correlation appears for comparison. It can be observed that the wedge angles do not lie directly on the theory line.

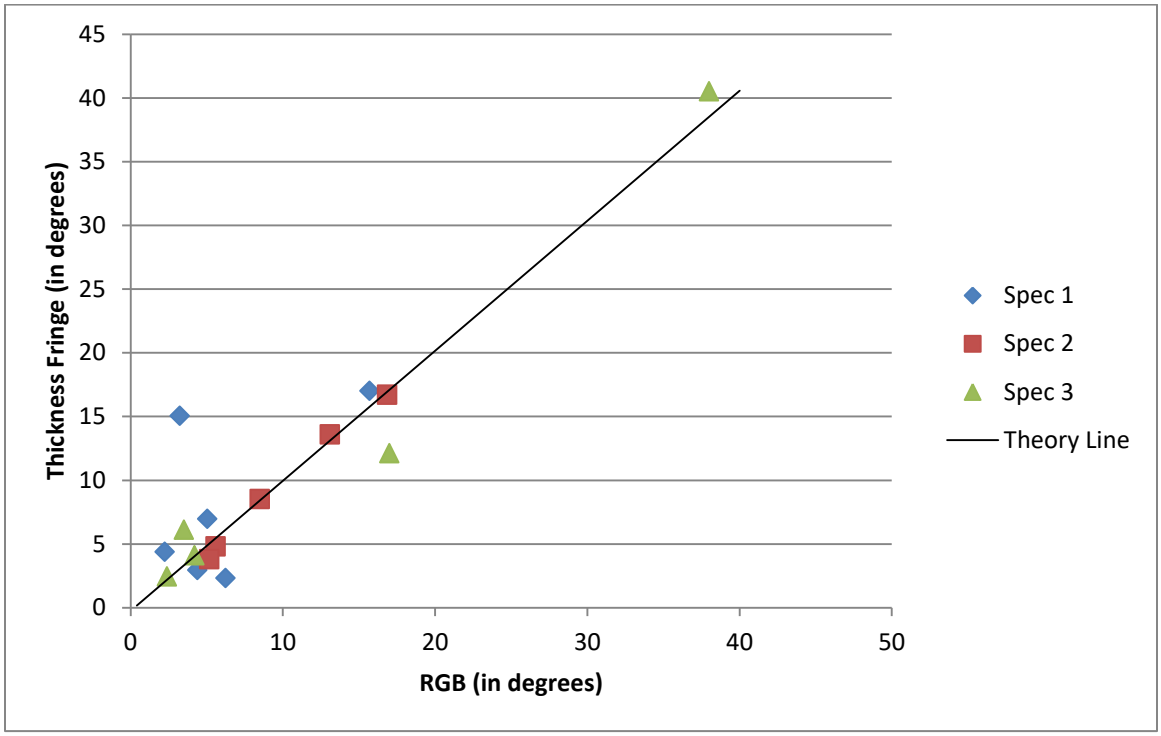

Figure 3.8: Graphical Comparison of RGB and Thickness Fringe Angles. Data from all three specimens and the predicted theory line

There are several possible reasons for the differences in wedge angle measurements between the two methods. First, the areas used for measurement are only approximations. Though it would be best to measure the exact spot in both cases, the reality is two different areas are being measured. This is because the AmScope

light microscope provides pixels to work with that are approximately 2 microns in scale. The TEM data is in the tenths of microns. So although data can be in the same general area, the exact approximation is much rougher than preferred. Second, the methods used to create and perforate each sample vary. For example, specimen 2 was created using ion milling, while specimen 3 was created through jet-etching. Ion milling subjects the sample to a much rougher process, and results in the creation of 'valleys' and 'peaks' on the sample along the perforation. These landmarks are on the submicron scale, and cannot be observed through the light microscope. However, the exact location- whether in a valley or on a peak- used when taking thickness fringe data in the TEM can cause a great variation on the outcome of the measured wedge angle. Jet-etching, by contrast, creates a much more uniform area around the perforation, but also leaves less large landmarks that can serve as reference points when approximating the same area in the light microscope.

Finally, the expected theory line might need adjustment. By probing deeper into the research of RGB analysis, it may be determined that the slope of the theory line needs to be adjusted from the slope of m=1 denoted in figure 3.8. With continued research, models of statistical variation will predict the scatter. The theory line used for this purpose is a rough preliminary line, and will be adjusted over time as the data gives us more information with which to work.

As the graphical comparison in figure 3.8 shows, the discrepancy between the RGB

and fringe estimations of thickness needs further investigation. Figure 3.9 looks at green and red ratios, and what they should theoretically tell us about specimen thickness. This plot seems to represent evidence that the previous analysis of how the color of transmitted light through silicon changes with increasing thickness is wrong, both from McCaffrey's data and data from this project. It appears that the red to green ratio does not increase with thickness. This observations in the figure might result from a phenomenon in older specimens that we can call "grey absorption." If images from specimens that have been decaying on a shelf had the excess grey values removed from the RGB values of each pixel, it is possible the data points on the figure would begin to fall closer to the theory line. As the addition of grey absorption would move the data points closer to the origin of the plot, the correction for this would move the points outward along a line through the origin.

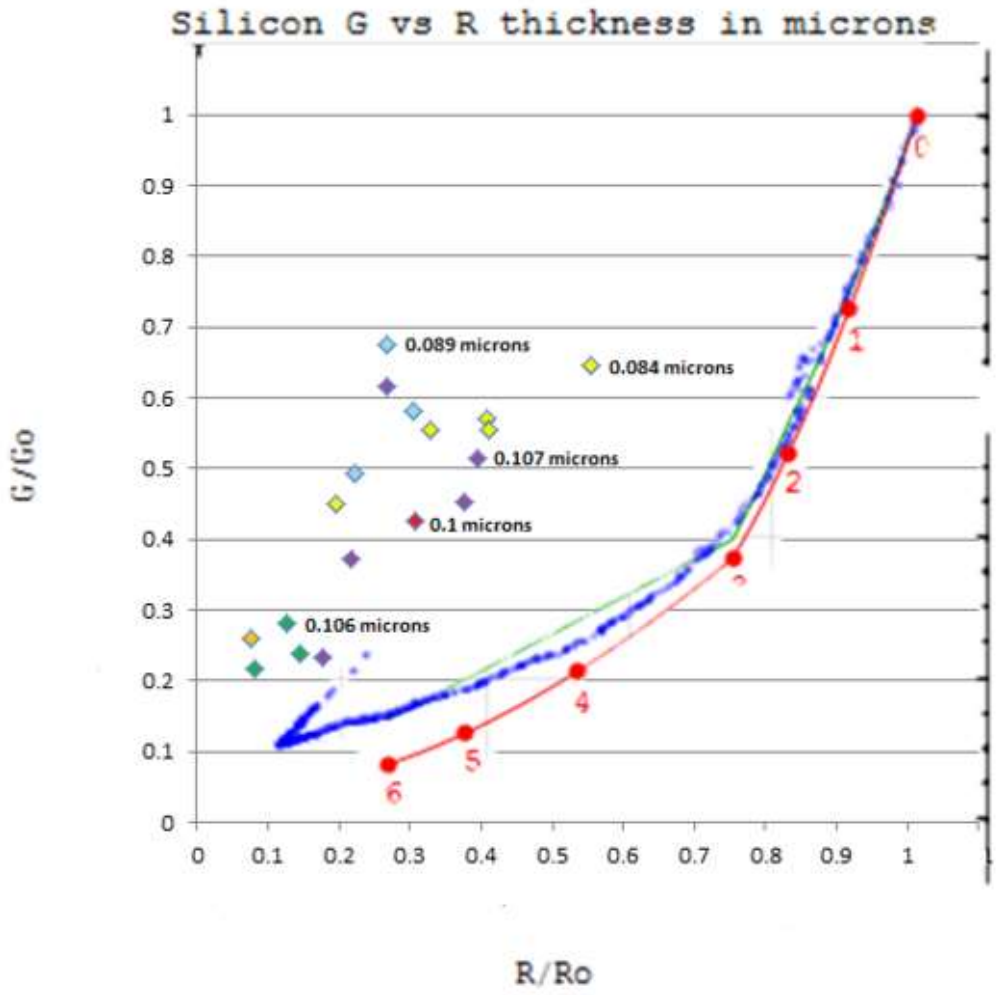

Figure 3.9: RGB Thickness chart with comparison points

To investigate this further, both newly prepared and old specimens were analyzed. In newly prepared specimens, specimen greying is less of a problem. Figure 3.10 shows a freshly prepared specimen and RGB profile, where the color changes clearly from white to yellow to orange to red and finally to black. However, in specimens that have "sat on the shelf" before analysis, greying skews the RGB values. Figure 3.11 shows an older specimen image both before and after the grey values have been removed, and their corresponding RGB profiles.

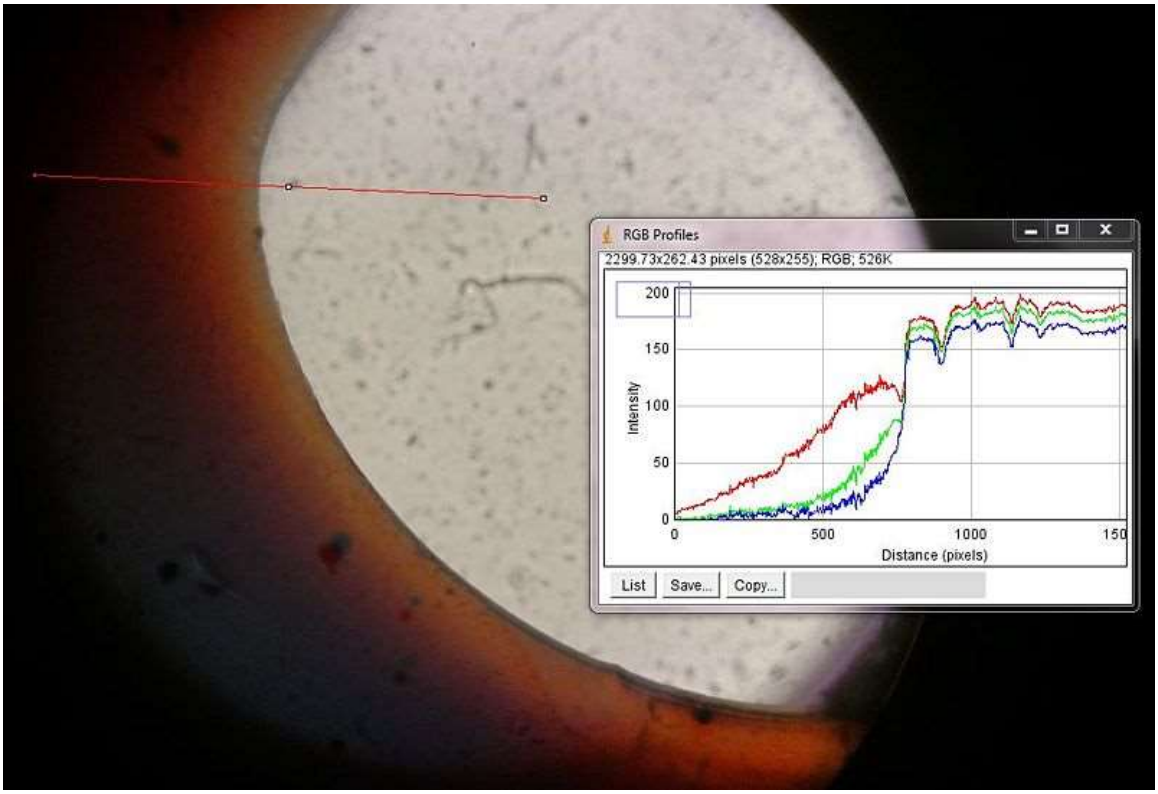

Figure 3.10: RGB profile along a line in a freshly prepared specimen

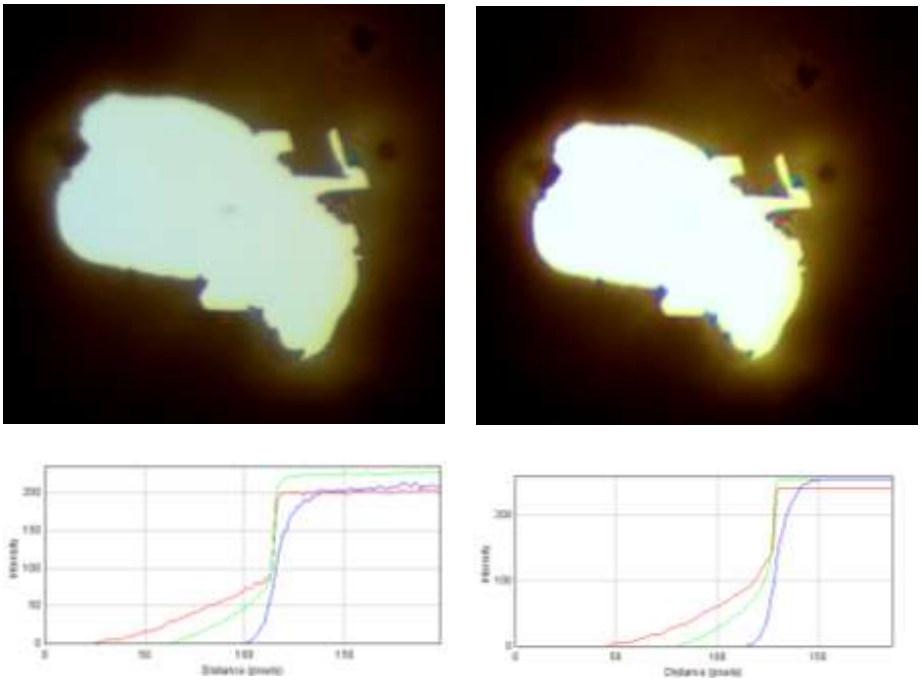

Figure 3.11: Specimen image and RGB profile before (left) and after(right) grey removal

Knowing that grey values are a potential issue, a closer look was taken at the McCaffrey model. Figure 3.12 shows sample images after the grey has been uniformly removed throughout the image, through ImageJ software. These images show a much better white to yellow to red progression than the original images, such as those in figure 3.3. Plotting the change in the green to red ratio with respect to moving further away from the specimen's hole, we can compare it to the McCaffrey data. Figure 3.13 shows that comparison. This graph plots pixel colors against the values of the McCaffrey data to show a qualitative change in the green to red ration as you move further away from the hole. The correlation is auspicious, as it shows that the greying of an image is effecting the data. After the grey removal, the mean error between McCaffrey's plot and the specimen plots was lowered to 0.0588 for the green to red attenuation.

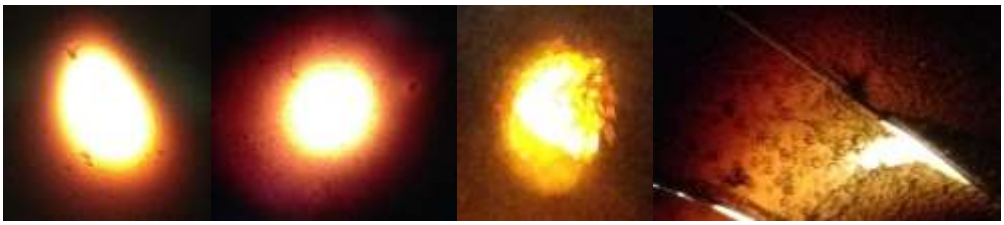

Figure 3.12: Specimen images with grey removed. From left to right: Specimen 6K-053-B4, Specimen GKF-064-04-2, Specimen 3509, Specimen 1

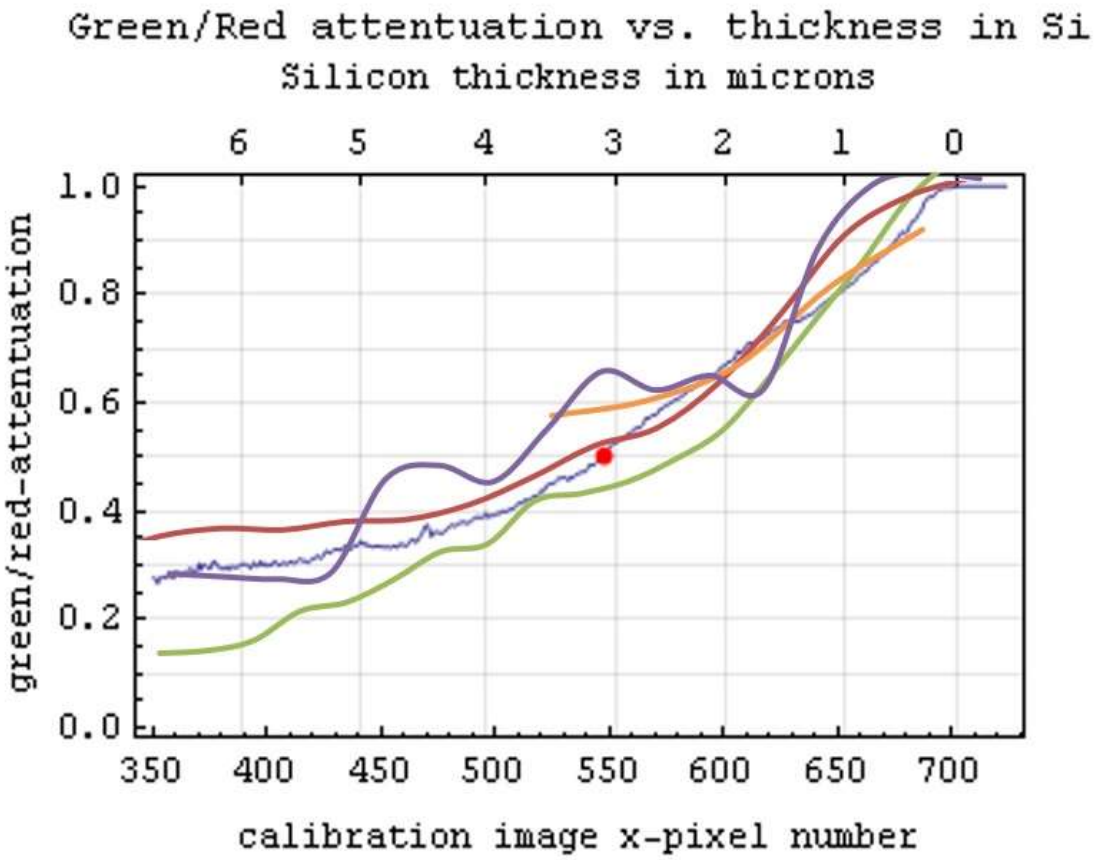

Figure 3.13: RGB vs. thickness comparison of grey-removed images and McCaffrey data. McCaffrey in blue, Specimen 6K-053-B4 in red, Specimen GKF-064-04-2 in green, Specimen 3509 in orange, and Specimen 1 in purple

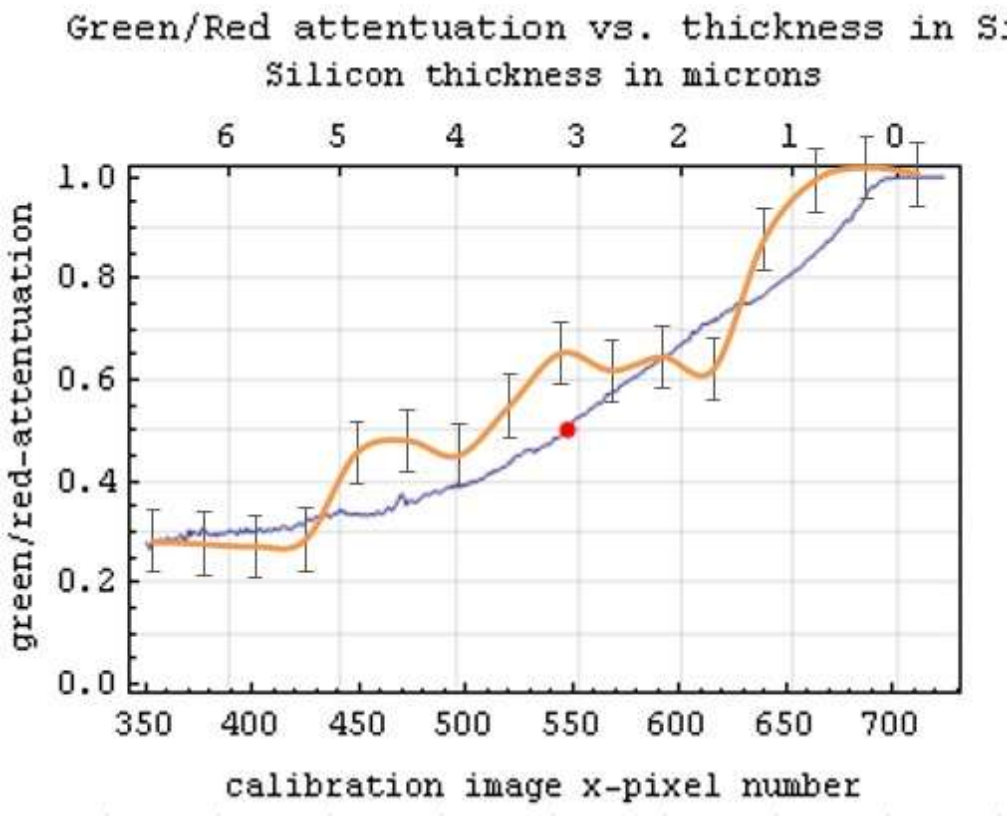

Figure 3.14: Comparison of Specimen 1 with McCaffrey, with mean error of 0.06 shown.

Specimen GKF 044-14 was analyzed after the grey values had been removed to compare with McCaffrey's data, using thickness fringes as a calibration method. The figures below show an initial analysis of the green and red ratios and the green to red ratio versus pixel distance along the line from the hole to the specimen. Next, RGB values are compared to thickness fringe data as a way to calculate thickness, with the specimen data detailed in figures 3.15 through 3.19. The results are plotted in figure 3.20. As noticeable from the graph, removing the grey value from the image corresponds to closer wedge angles calculations.

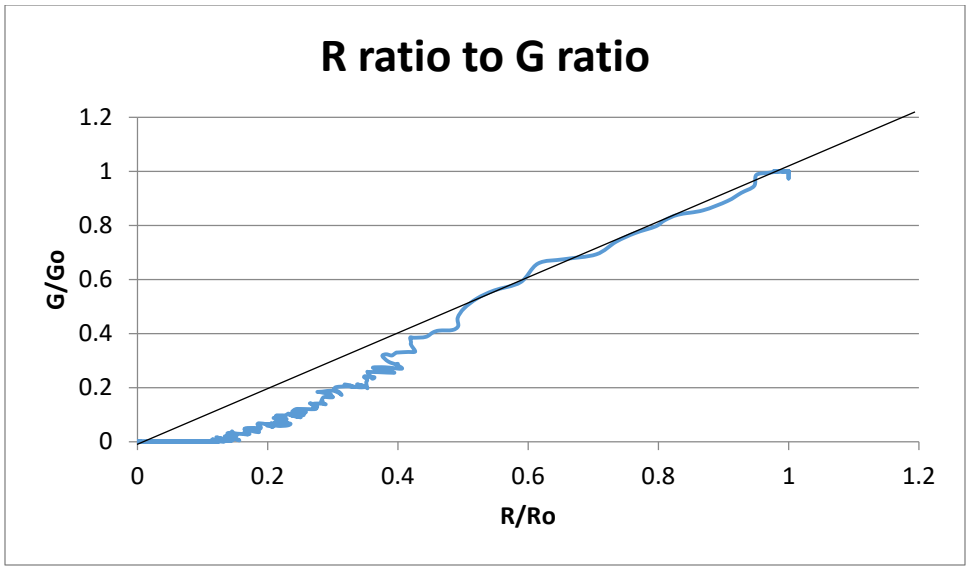

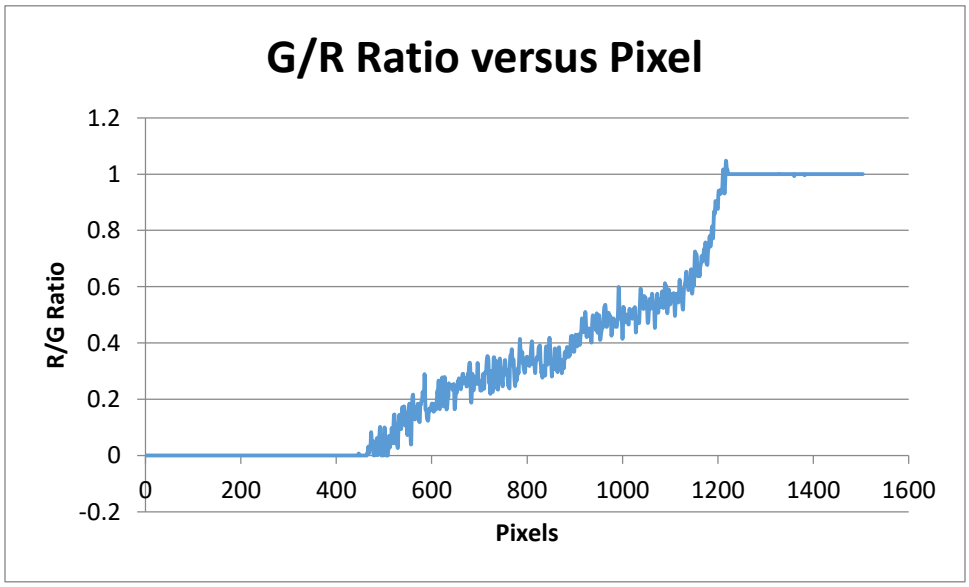

Figure 3.15: Green to red ratio (top) and color ratio change with thickness (bottom) for GKF 044-14 after grey-removal

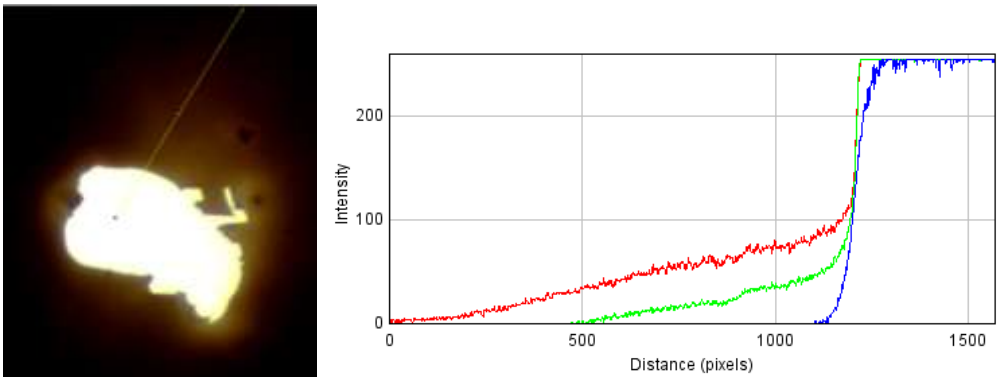

Figure 3.16: RGB profile (right) for area 5046 in specimen GKF 044-14, marked at left

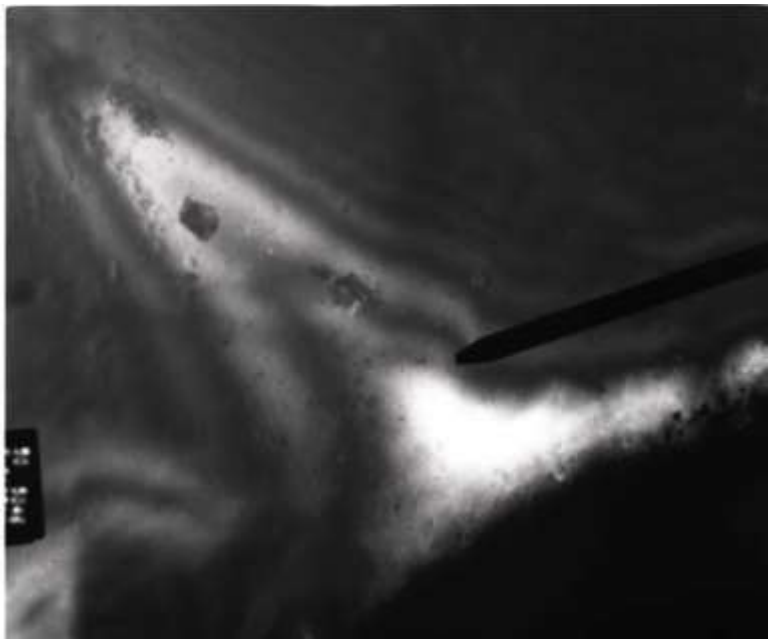

Figure 3.17: Thickness fringes for area 5046 in specimen GKF 044-14

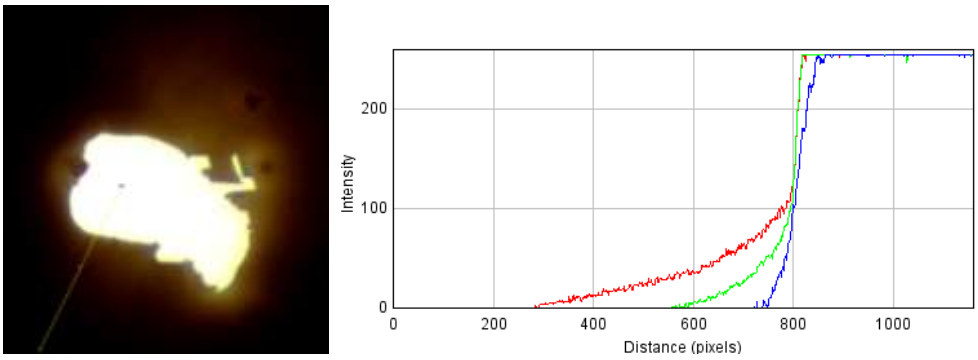

Figure 3.18: RGB profile (right) for area 5047 in specimen GKF 044-14, marked at left

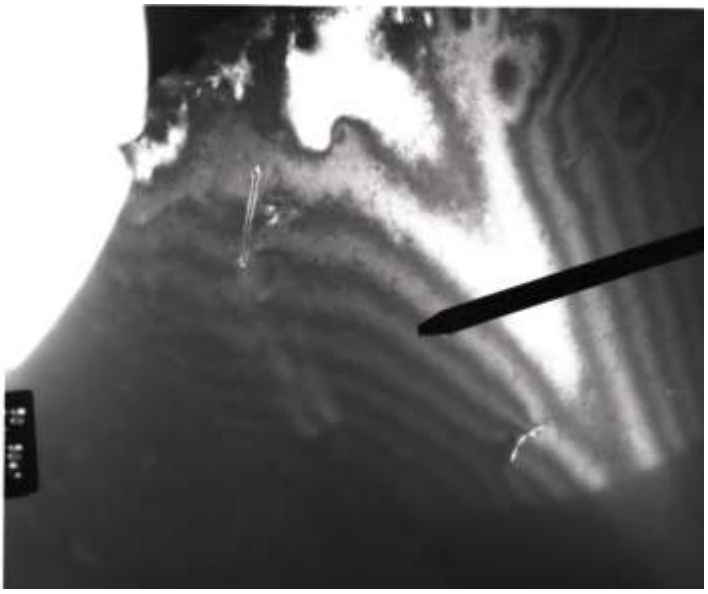

Figure 3.19: Thickness fringes for area 5047 in specimen GKF 044-14

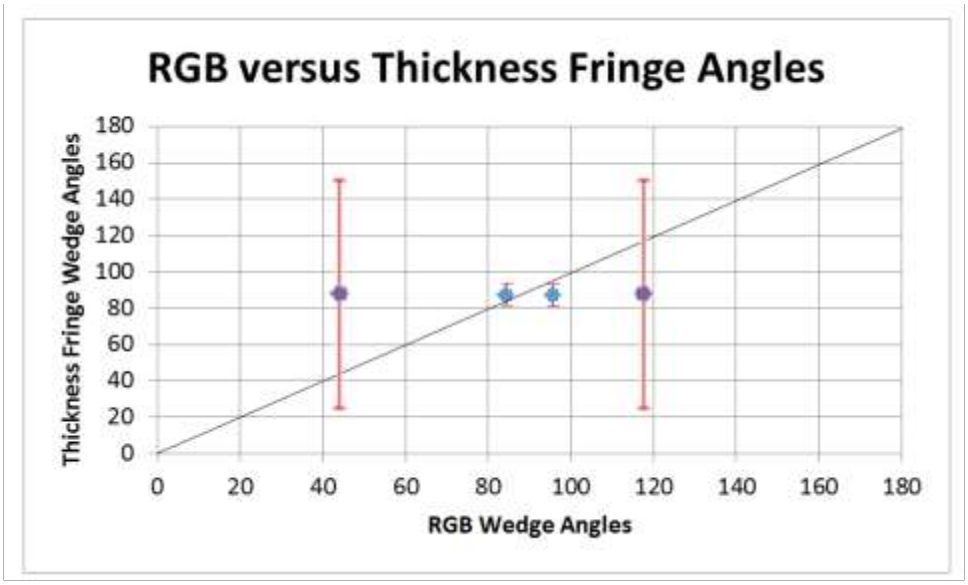

Figure 3.20: Comparison of thickness from RGB and Fringe method for areas 5046 and 5047 in specimen GKF 044-14. Original image data in purple, and grey-removed data in blue.

Another source of errors, outside of the added grey values in the image, can be found from the conditions in which the image was taken. The tilt of the camera, and the reflection of room lights can both add to changes in the expected thickness values. An examination of such sources of error is plotted in figure 3.21. This included investigating the RGB thickness value changes to specific regions of a specimen when three conditions were implemented: room lights on, room lights on and the camera tilted to an angle, and room lights off with the camera tilted to an angle. The six specimens used for this investigation were Specimen GKF-064-13-3, Specimen GKF-064-16-2, Specimen GKF-064-04-2, Specimen HMF-064-51-1, and Specimen GKF-060-7-16. As the graph shows, no clear shift is readily apparent from each variation, i.e. the red and green values get higher (shift toward

white, the average value found in the hole), when room lights are added. Thus, more investigation is needed on how to adequately account for variations in the method of data collection when looking for thickness values from RGB analysis.

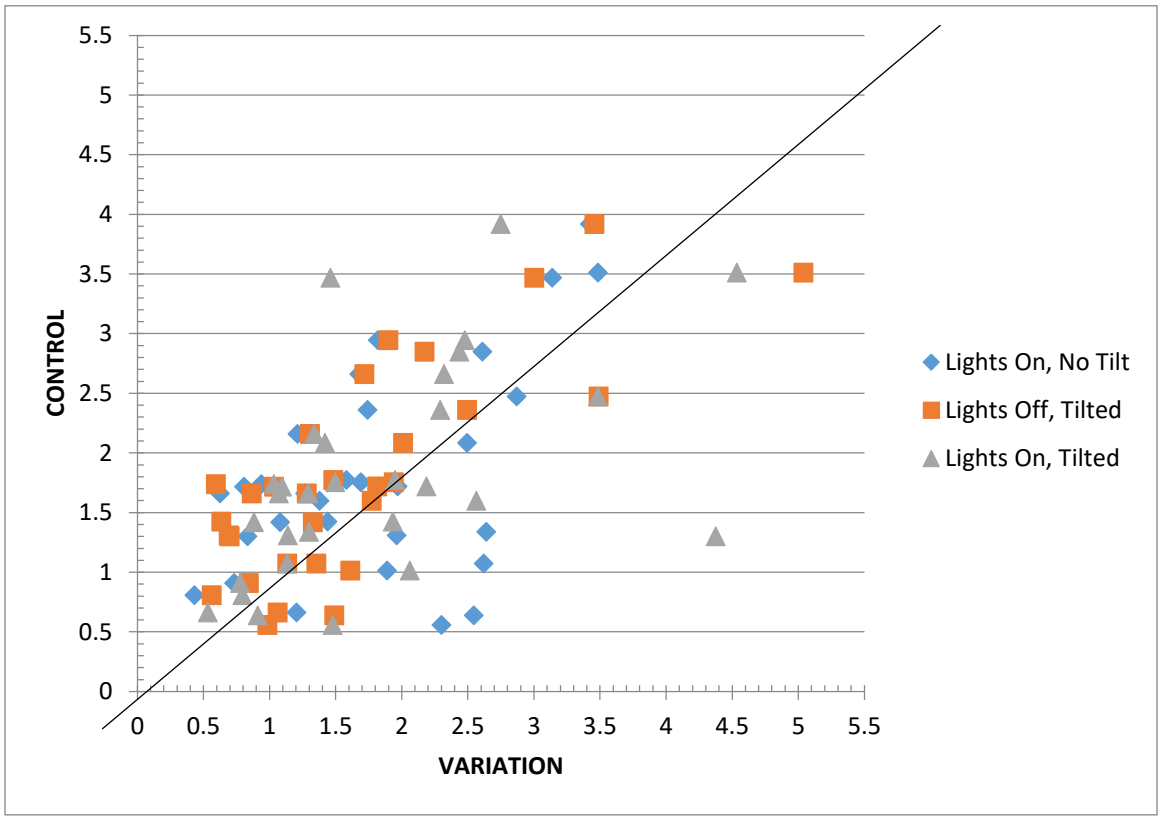

Figure 3.21: Control vs variations for RGB thickness calibrations

Through examination of the results from this method and the comparison of outcomes from other methods, it is clear that this method of analyzing wedge angles in perforated silicon specimens is a valid technique, but could be improved to reduce errors, coming from a variety of sources. This approach to calculating wedge angles seems both fast and moderately reliable from this preliminary analysis, and can be used as an effective mode of acquiring results.

4 Oxygen Related Defects in Silicon

In this part of the project, oxygen in Czochralski-grown silicon for the solar cell and semiconductor industries is examined. The resulting oxygen precipitate platelet cluster distribution variances throughout an ingot, Boltzmann-factor visualizations of sub-critical cluster distributions in the solid-state, and strategies for exploring these topics in the TEM are then discussed.

In order to accurately characterize specimens, the best methods of preparing samples must be explored. These methods will deliver the required results while minimizing damage and residual effects on the specimen. The silicon samples prepared in this research were 3 mm discs cut from Czochralski-grown (Cz) silicon wafers. Preparation methods explored include annealing, ion milling and tripod polishing for the transmission electron microscope (TEM).

4.1 Oxygen Defects Background

4.1.1 Annealing

The use of heat treatments on specimens has several purposes. One purpose is for securing photoresist to the specimen, while a different use is bonding a specimen to another specimen or material, both techniques used in the thin film preparations for this project. Another is to obscure or amplify material differences through temperature-related diffusion. Annealing was used for Cz silicon as a method of causing oxygen precipitation, and thus a distinction between oxygen clusters in various locations of an ingot. Annealing times varied from 30 minutes to 48 hours. Clean annealing processes were unavailable in the research facilities utilized for this

project, but an attempt was made to limit contamination as much as possible. This included the use of a new quartz oven tube and small specimen quartz tube, used only on anneals for the specific materials used in this project. Also, the specimens were covered in small Si balls to try to minimize diffusion of contaminants into the specimen disc. This was later determined to be ineffective, but to conserve uniformity in specimen preparation, there use was continued. In figure 4.1 below, the specimen tube with silicon balls and the oven are depicted.

Figure 4.1: Cz Si disc in clean quartz tube surrounded by small Si balls (left). The oven in the Advanced Physics Laboratory used for annealing specimens (right).

4.1.2 Ion Milling

Though it is the industry standard for specimen preparation, ion milling seems to produce certain constraints when looking at silicon. Previous work shows that there is indeed a problem with the ion mill technique when looking at early stage oxygen cluster formation in silicon, since small surface-inclusions form when the samples are exposed to oxygen. However, the work also shows that detecting small unstrained clusters is possible. [2] The two basic limitations for this type of specimen preparation that concern this project are strain contours around the thin

area of the perforation and the creation of unstrained oxygen cluster surface intrusions upon exposure to air. The strain contours remove thickness fringes and make thickness characterizations more difficult, and additional oxygen clusters on the surface may skew data and make defects under 10 nm uncountable in the data, as their origins could be rooted in the ion milling process and not the interstitial oxygen abundance of the original material.

Thus, ion milling and transporting in air is a major issue and thickness fringe data on these specimens is unreliable due to wiggly silicon around perforation edges and user error in determining the Bragg condition, eliminating their use as a method for characterizing thickness. The estimated searchable volume for an ion milled specimen is 31,390 μm^3, and the searchable surface area is 12,415 μm^2. These values were derived by assuming a 15 mm diameter of the dimpler wheel, giving a uniform perforation of approximately 200μm, a maximum thickness of 5000Å and a wedge angle of 1.5°. The calculations used are shown in figure 4.2. Note diameter must be changed into circumference to use these wedge calculations. Future work on the subject of ion mill artifacts in Cz silicon is being considered by the author.

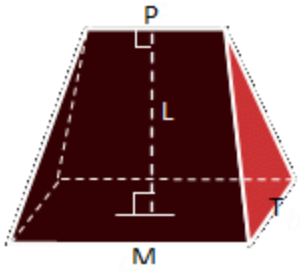

P: Perforation Diameter = 200 microns
M: Max Thickness Diameter = 214 microns
T: Thickness = 1/2 micron
L: Length = 19 microns

Volume = (TL/6)(2M+P)
Area = L(P+M)/2

Figure 4.2: Top: Ion Mill Wedge Calculations diagram. Bottom: Ion Mill (left), Cz silicon specimen on holder and in ion mill bay (center), View of perforation through ion mill microscope (right)

4.1.3 Tripod Polishing

Tripod polishing is another method for specimen preparation. This method utilizes mechanical thinning at an angle to create a thin edge on one side of the specimen. For this method, one must prepare relatively large wedge angles (~4^{o}) to prevent the specimen from exhibiting 'wiggle' when viewed in the TEM. But, creating large wedge angles also lowers the potential thin area to search. The estimated searchable volume for a specimen prepared for the TEM through tripod polishing is 11,760 μm ^{3}, and the searchable surface area is 4,645 μm ^{2}. These values were derived by assuming the same values as in the calculations for ion milling, except a wedge angle of 4^{o}. This method is currently being explored as an alternative to ion milling

for the purpose of viewing specimens in the TEM without the oxygen surface cluster intrusion artifacts produced through ion milling and exposure to air.

4.2 Oxygen Defects Methods

4.2.1 TEM Metrology Strategies

In this part of the project, the limits on solar and device grade single crystal Czochralski (Cz) silicon, whose oxygen content from the quartz crucible used to hold the melt, reported by Sun Edison Solar, is at the 5 to 20 ppma level, or ~10^{18}/cc. This is orders of magnitude above that of the electrically active dopant used to decide the majority carrier type. This project's particular focus is on oxygen precipitate number density in industry-grown silicon wafer regions, as a diagnostic of process-related differences from one specimen to the next.

For this project, a 2D grid search for oxygen precipitates was implemented in a 3mm-diameter ion-mill perforated TEM planar-section specimen of (100) Cz silicon and its secondary defects (prismatic dislocation loops, dislocation tangles, and larger (micron-sized) extrinsic stacking faults). A perforation wedge-angle model of specimen thickness, calibrated with the help of large (111) stacking faults in this specimen, allowed for examination of the surface area to volume correlations for the defects, as well as the estimation of precipitate volume density. The result agreed with other density measurements and model predictions (~10^{11}/cc) within an order of magnitude. With additional work and computer support, this analysis can

be done in real-time in the electron microscope, where data may be possible to take as needed to get the uncertainties in hand.

For the process, a planar-section TEM specimen of Cz silicon under study with collaborators at Sun Edison Solar, most of whose oxygen had been precipitated by nucleation and growth heat treatments, was used to explore the challenges of defect density-measurement. The specimen was a 3mm diameter disk with an approximately 400 micron diameter argon ion-milled perforation in the center. Separate observations and models had already indicated oxygen-precipitate densities in the 10^{11}/cc range.

The thickness for the surveyed regions was needed to investigate the volume number-density of the oxygen precipitates. Two methods were used to find this information. The first was a digital red/green/blue (RGB) analysis using differential photon absorption in the specimen to determine the wedge angle around the perforation, discussed in chapter 2. The second method for determining sample thickness in a given region was through the use of stacking fault defects in the material, also considered in chapter 2. The purpose of using the two methods was to begin calibrating the RGB method, a technique whose accuracy has yet to be determined, with the accepted accuracy of the geometric-based approach that verifies thickness through stacking faults.

Finally, oxygen precipitates were located and categorized in the sample via a systematic grid search of regions by tilting under dark field imaging conditions. In this way, strained lattice planes associated with a 220 or 400 reflection would light up, just away from the Bragg condition for the lattice. By employing this process, several regions of the sample were viewed, and data on the defects and their locations was collected and categorized. Because the microscope's dark field cluster controls were used to set up search conditions, rapid switching between bright-field and dark-field image modes could also be used to help clarify defect identifications.

The grid search was meticulous. A region of the thinned specimen was identified by a distinguishing characteristic, and a sub-region field of view (FOV) matrix, spanning this region, was defined bordering the edge of the perforation. Total area examined was calculated based on the TEM magnification at which each field spanned the width of the microscope's viewing screen. Each specimen region was examined under both bright field and dark field contrasts over a range of tilts around the Bragg condition, which caused the silicon matrix to "light up" in dark field, giving location information on each precipitate to record. Figure 4.3 shows example of a grid search area, where the specimen is in white, the perforation is in black, and the green circles each represent one FOV. Once all defects in the FOV were recorded, the microscope was carefully moved to an adjoining FOV with the use of landmarks on the specimen and the precipitate identification process was repeated. The FOV matrix extended as far from the perforation edge as possible,

until imaging became too dark to classify defects as a result of multiple scattering. The resulting grid search information on precipitates and locations was charted in a spreadsheet.

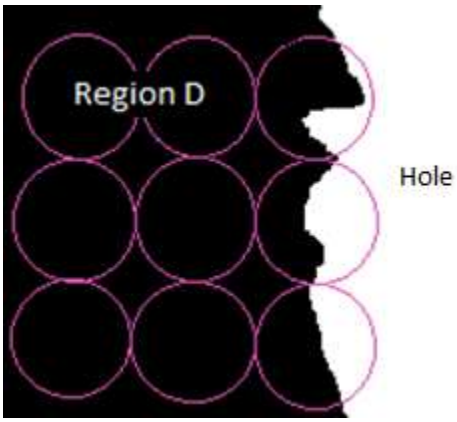

Figure 4.3: Example field of view matrix, with the perforation white and material black. Each magenta circle represents one field of view.

Precipitate identification involved matching crystallographic defects found in the grid search with images of previously identified defect types. Figure 4.4 and figure 4.5 are identification images of various types of precipitates used for this purpose. The square platelets, figure 4.5, can be identified as shown only one-third of the time. This is because there are three {100}-type planes in the silicon lattice, so they will be seen edge-on, as opposed to face-on, the rest of the time.

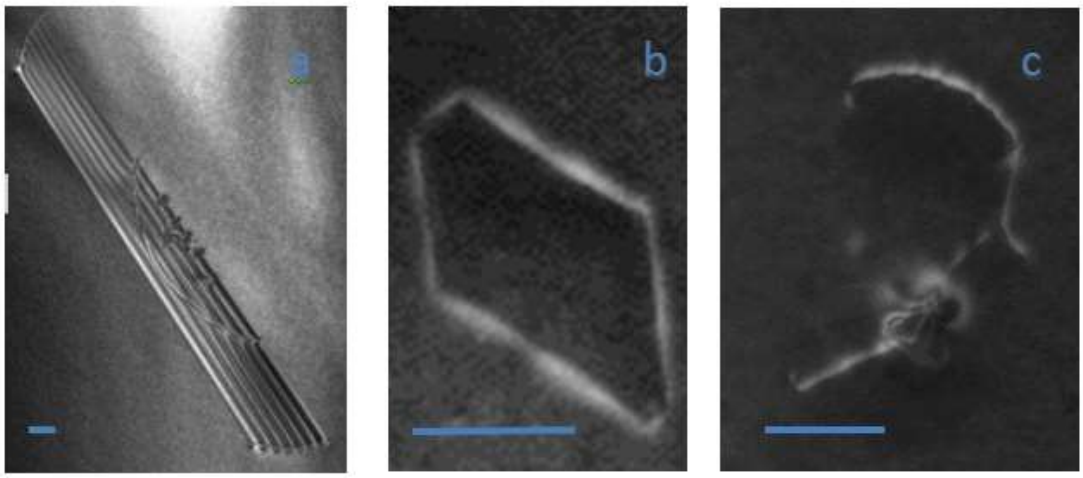

Figure 4.4: Precipitation Identification Images, courtesy of D. Osborn: All scale bars are 200 nm. (a) stacking fault intersecting top and bottom specimen surfaces, (b) prismatic dislocation loop, (c) precipitate-dislocation complex (PDC)

Figure 4.5: Image of a square platelet lying in a (100) plane perpendicular the beam direction. [21]

To identify precipitates, the location information for each was used to go back to the position. Once there, the magnification was increased until the precipitate could be identified, and the type was recorded. It is important to note that not all precipitates resembled the images in figures 4.4 and 4.5 as the appearance of the precipitate depended on its orientation in the lattice plane. For example, figure 4.5

shows a platelet face on, possibly on the { 1 0 0 }orientation, whereas those at an orientation of < 0 1 0 > or < 1 0 0 > would have a linear appearance. For some precipitates, the length and width was recorded. To help with data analysis, the sizes of all precipitates should be recorded in any future grid searches. The dimension of the precipitates was approximately 570 Å.

The data obtained from the specimen 6K-058B4 1420 was analyzed to find the wedge angle for several regions. First, the RGB method was used. The equation for wedge angle analysis from differential photon absorption in silicon is as follows:

$$Thickness \cong 6.58 - \sqrt{60.6\left(\frac{G}{R}\right) - 17.4}$$

$$\frac{G}{R} \equiv \left(\frac{\frac{G}{G_0}}{\frac{R}{R_0}}\right)$$

Following the procedures outlined earlier, values were calculated for several regions and used to find an average. Next, thickness and wedge angle measurements were calculated using stacking fault defects found in various regions of the specimen. The wedge angle, Θ, is given by the following expression:

$$\theta = tan^{-1}\frac{\sqrt{2}w}{L}$$

Here, w is the width of the stacking fault and L is the distance to the perforation. The wedge angle results are listed in Table 4.1, along with the potential error. From these measurements, an average wedge angle for the specimen is approximately 2.79 degrees.

	RGB Thickness	RGB Length	RGB Wedge Angle (Degrees)	Stacking Fault Thickness	SF dist. from hole	SF Wedge Angle (Degrees)
Region A	NA	68.63 μm	NA	362 nm	12,670 nm	2.31
Region B	NA	38.21 μm	NA	.225 mm	6.8 mm	2.68
Region C	NA	50.64 μm	NA	NA	NA	NA
Region D	2.5 microns	46.00 μm	3.11	1086 nm	20,815 nm	4.22
Region E	1.9 microns	41.55 μm	2.62	489 nm	19,910 nm	1.99
Region F	NA	39.51 μm	NA	362 nm	12,670 nm	2.31
Average			2.87			2.7
Total Average:		**2.79**				

Table 4.1: Calculated wedge angles of specimen 6K-058B4 1420

4.2.2 Detecting Oxygen Defects

Two Sun Edison wafers, P04KT-C9-SE5 (corresponding to the seed end of an ingot) and P04KT-C9-OE3 (corresponding to the opposite end, or tail, of an ingot), were subjected to a 12-hour industry heat treatment at 950 °C. From there, small 3mm discs were cut from the wafers, thinned, and perforated through double sided ion milling. Under high magnification in the TEM, each specimen was examined by eye for bulk defects. Strain fields and orientation of structures were two ways used to determine if objects of interest were oxygen defects or not. Both bright field and dark field contrasts were used, and the thin area around the perforation was searched, as described in the last section. The first specimens examined for bulk defects were considered "as received," with no secondary heat treatment. Specimen

P04KT-C9-SE5 has a given oxygen number density near 10^{18} oxygen atoms per cubic centimeter, meaning there is plenty of oxygen to cause defects to look at under the TEM. Yet, bulk defects were difficult to detect in the TEM in the "as received" specimens. After three hours of surveying the specimen at 35kx, it was determined that no bulk defects were visible. Oxygen precipitates were still unstrained, and further heat treatments were required.

A secondary anneal was needed in order to cause the oxygen to precipitate, causing strain in the lattice and thus creating visible defects to observe. However, the heat treatment must be carefully selected to develop discernable defects while not obscuring the differences between specimens coming from varying wafers, ingots and radial locations. Table 4.2 shows the specimens and their subsequent anneals.

Seed End Specimens	Anneal	TEM Observations	Opposite End Specimens	Anneal	TEM Observations
P04KT-C9-SE5 Center Cut 1	Industry anneal only	No visible precipitates	P04KT-C9-OE3 Center Cut 0	Industry anneal only	not searched
P04KT-C9-SE5 Center Cut 2	20hr anneal	15,000 nm^3 searched, defects detected	P04KT-C9-OE3 Center Cut 1	20hr "copy cat" anneal	27,500 nm^3 searched, defects detected
P04KT-C9-SE5 Center Cut 4	(A1) 12hr double anneal	39,500 nm^3 searched, defects detected	P04KT-C9-OE3 Center Cut 2	(A1) 12hr double anneal	17,700 nm^3 searched, defects not detected
P04KT-C9-SE5 Center Cut 5	(A2) 24hr double anneal	no detectable difference to 20hr	P04KT-C9-OE3 Center Cut 3	(A2) 24hr double anneal	not searched

Table 4.2: Specimen chart

From these experiments with anneals and subsequent searches in the TEM, it became clear that a better model was needed to predict oxygen cluster behavior in silicon during various heat treatments. In the real world, calculating such behavior would require simulating the system with methods such as the Monte Carlo method, but a more generalized behavior may be adapted for the purpose of this research. At high temperatures, the diffusion constant $D=D_{De}^{-\epsilon/kT}$, which is temperature dependent, allows oxygen high mobility. After considering the thermal history of the specimen in the puller and the supersaturation point, it was determined that the

best chance of precipitating the oxygen in the sample was by prolonging the heat treatment in the 600-950°C range to take advantage of precursor cluster formation.

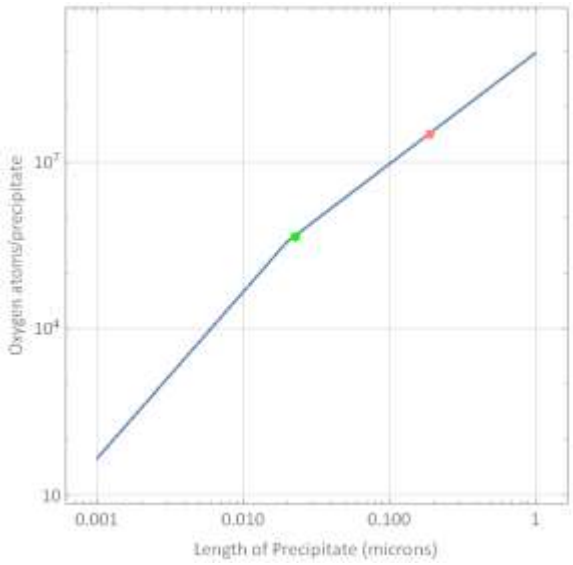

Figure 4.6: Precipitate size- a first look

In figure 4.6, the red dot corresponds to a heat treatment at 950 of the industry 12 hours plus an additional 20 hours, while the green dot corresponds to a heat treatment at 950°C of the industry 12 hours plus an additional 12 hours, both calculated from average platelet lengths in TEM images. Given an average observed value of 3 precipitates per cubic centimeter, and estimating the specimen thickness to be 2000Å, then

$$\frac{\#}{volume} = \frac{10^5\ prec/cc}{2\ x\ 10^{-5}\ cm} = 0.5\ x\ 10^{10}\ \frac{prec}{cc} \sim 5\ x\ 10^9\ \frac{prec}{cc}$$

This number is within the given industry estimate of 10^9 to 10^{11} prec/cc (depending on proximity to the center of the ingot). That means that any given oxygen atom

would have to travel a distance of approximately 1,250 nm before encountering a precipitate to which it can cluster. Between that and known diffusion behaviors of oxygen in silicon, the specimen would need to spend approximately 35 hours at 950°C to allow for the nucleation of approximately 10^{11} atoms of oxygen. However, after only 12 more hours of additional heat treatments, oxygen precipitates were visible under the TEM. A defect count of 19 was found in an area of approximately 1.96×10^{-2} cm^2. The estimated defect count for such an area from the oxygen approximation was 20, showing an error of $\frac{1}{20}$ or 5%. However, no defects were found for the opposite end specimen both after first surveying under the same magnification, and then moving to a higher magnification of 350kx. Figures 4.7 and 4.8 show TEM images of oxygen precipitates in the specimens.

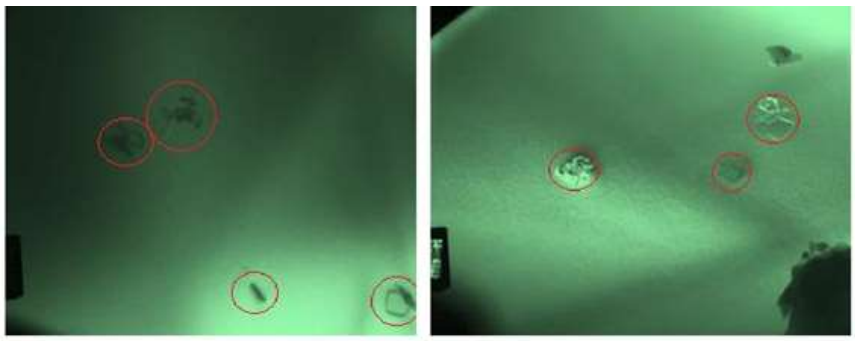

Figure 4.7: Oxygen precipitates in P04KT-C9-SE5 (2) (left); Oxygen precipitates in P04KT-C9-SE5 (4) (right). Oxygen precipitates marked with a red circle

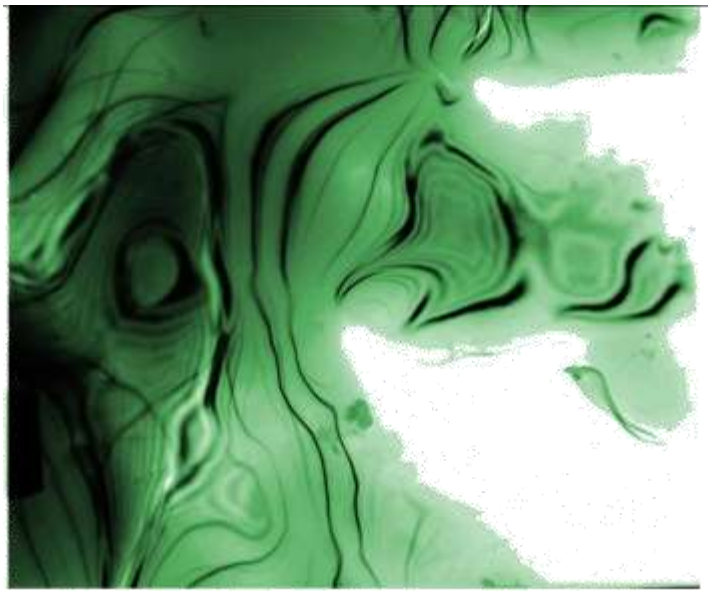

Figure 4.8: Oxygen precipitates in P04KT-C9-OE3 (2). Contour lines illustrate a healthy silicon specimen with no precipitates being illuminated by tilting contrast mechanisms.

This suggests that strained-precipitate formation is suppressed in the center of an ingot at the opposite end, relative to seed end, in silicon wafers. This could be the result of the shorter time the opposite end of the specimen spends in the precursor-phase nucleation temperature range between 600°C and 800°C. If this difference is also connected to the observed differences in minority-carrier lifetimes in the opposite end of wafers, then a pre-anneal of the that end of the specimen, again in the 600-800°C range should both reduce minority-carrier lifetime and increase precipitate formation following any subsequent 950°C anneals.

A second seed-end specimen, P04KT-C9-SE5(7) cut annealed and prepared in the same way as the specimen above (P04KT-C9-SE5(2)). Finding 34 precipitates in

63 fields of view at a magnification of 8kx, the precipitate number density of the specimen is approximately 10^{10} prec/cc, confirming the validity of precipitate density of this part of the wafer to be within industry standards. Figure 4.9 shows some precipitates from this specimen.

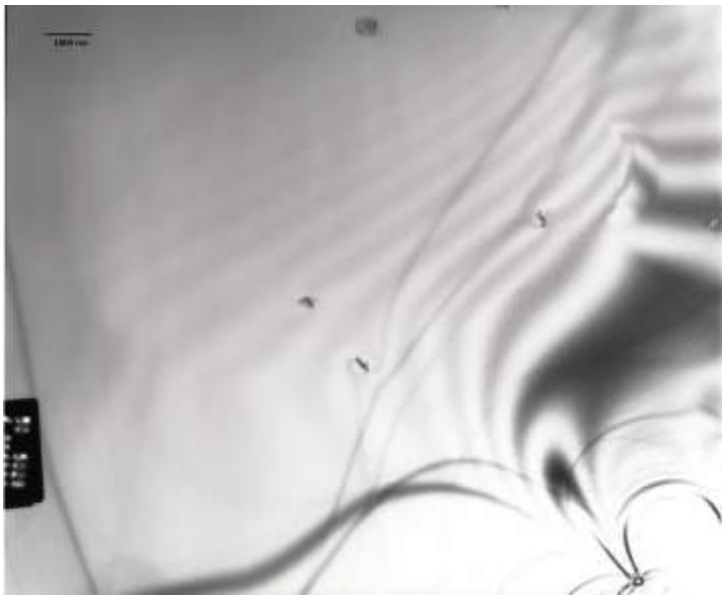

Figure 4.9: TEM image of precipitates in P04KT-C9-SE5(7)

4.3 Oxygen Defects Results

4.3.1 TEM Metrology Strategies

From the grid search performed on the specimen, the number of precipitates versus distance from the hole was calculated, using counting statistics for the error and assuming that the defects were Poisson distributed. The results are shown in figure 4.10 below. Most precipitates categorized lie between 5000 nm and 10,000 nm from the perforation, though this is likely due to loss of diffraction contrast information in TEM images as the specimen thickness increases.

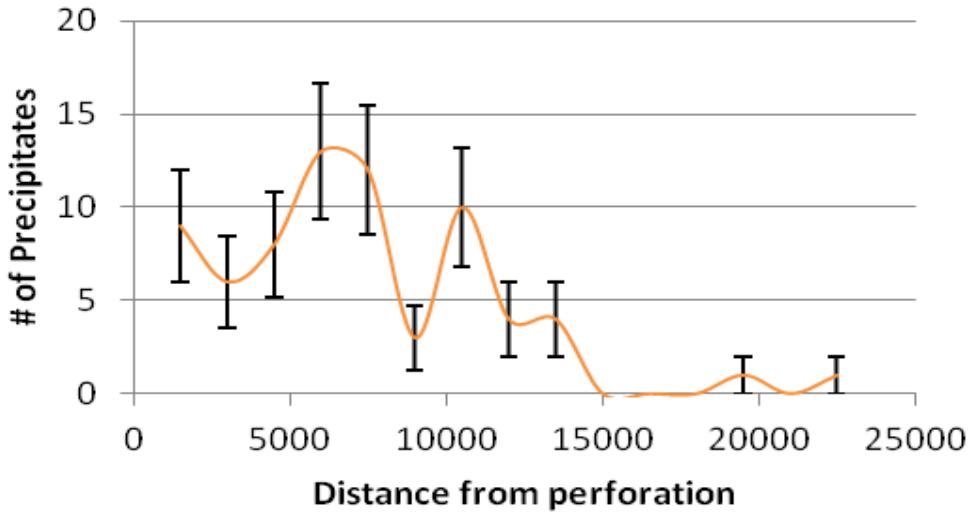

Figure 4.10: Precipitates versus perforation distance (in nm)

Each precipitate was categorized into a type. The four categories consisted of stacking faults, precipitates, dislocation loops, and other (such as fragments, partial dislocations, etc.). The percentage of each is listed in table 4.3.

Type of Defect	Number of Precipitates	Percentage of Precipitates
Stacking Fault	1	1%
Prismatic Dislocation Loop	19	27%
Precipitate with Secondary Defect	40	56%
Bulk Defects Not Clearly Identified	11	16%

Table 4.3: Lattice defect types

Precipitate number density was estimated from 71 identified precipitates in 24 FOV. This equates to 2.96 precipitates per FOV. Therefore, with an estimated volume of 1.22×10^{-10} cubic centimeters, the resulting precipitate number-density estimate was 2.42×10^{10} precipitates per cubic centimeter. On average, the thickness that can be searched in the TEM ranges from a few angstroms near the perforation to a half-micron, where the specimen becomes dark and inelastic scattering washes out the diffraction contrast needed to identify precipitates. The specimen thickness of a given area could most accurately be determined through stacking fault measurements, and thus those calculations, along with the FOV dimensions, were used to obtain volumes for each region searched.

This method of sample characterization through TEM imaging works well for characterizing: (i) individual precipitate and secondary-defect structures in the sample, and with added work also (ii) the *distribution* of sizes and locations of each type with respect to the perforation in a prepared specimen. The results above are from only about 2.37% of the thin area of that perforated specimen. The number of defects per unit volume was determined to be in the 10^{10} to 10^{11} range, as it uncovered a precipitate density of 2.42E10, or about 24% of the predicted value of 10^{11}.

The plot in figure 4.11 of experimentally observable quantities for a wide range of applications, namely the maximum object-dimension versus the number of objects per unit volume, is useful in understanding the challenge of statistical sampling via

TEM observation. Smaller-defects require higher magnification and hence smaller fields of view, while lower number-densities increase the amount of volume that must be surveyed to get a statistically representative sample. For example, this initial survey identified 71 oxygen precipitates in 51 fields of view at 19.5kx, in a surveyed volume of 1.7 10^6 cubic microns. Smaller precipitates with the same number density (represented by bottom of the cyan line in the figure), due to less total oxygen precipitated, might have required higher magnifications and hence more field of views for the same statistical significance.

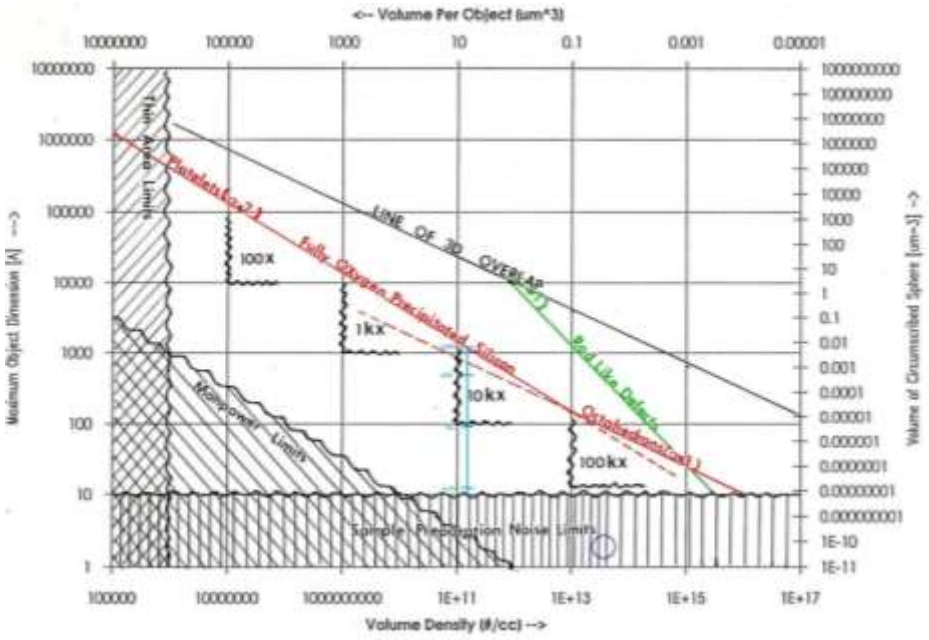

Figure 4.11: Defect maximum-size versus volume-density map: Our observed volume density is marked with range-bars in cyan near the center of this figure from an earlier paper on TEM metrology. [13]

A second plot (in figure 4.12) of experimentally observable quantities, namely the maximum object-dimension versus the number of oxygen atoms per precipitate.

Three stage model plot, formatted to overlay on log-log plots of experimental TEM/FTIR data about oxygen precipitation in electronic grade silicon. The number of oxygen atoms per precipitate at transitions (green and red dots on the plot) have here been inferred from previous observations in the literature, but expect will, in general, depend on prior thermal, point-defect, and impurity history. [14] [15] This has long been part of the work toward semi-empirical models of oxygen in silicon. This is because one would expect the number of oxygen atoms per precipitate, at which various shape transitions occur, will (along with the number density of precipitates itself) be sensitive to point defect and impurity concentrations through a wafer's prior thermal history. Another active goal of this project, for future reports, is to help refine existing semi-empirical models for these dependencies.

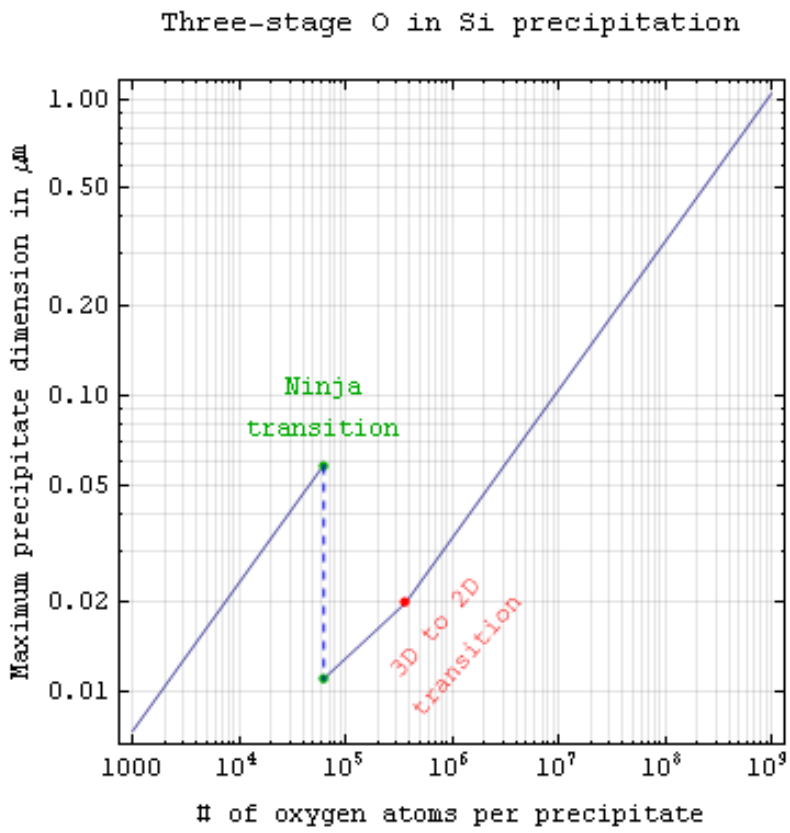

Figure 4.12: Three stage model plot with an inferred number of oxygen atoms per precipitate at transitions

4.3.2 Further Explorations of Oxygen Clusters

To further explore precursor-phase nucleation, critical cluster size as a function of temperature in silicon was investigated. Using 10^{18} Oxygen/cc as a starting concentration, the given industry standard, C_0 (critical size of clusters) can be computed through the following simplified equations:

$$n_{critical} = \frac{32\pi\sigma^3}{3v|\Delta G|^3}$$

$$\Delta G = -kT\left\{log\left(\frac{C_0}{Solubility}\right)\right\}$$

A calculated range of critical sizes for certain temperatures needed to make a cluster stable is then:

Temperature (°C)	600	700	800	900	1000
Critical Size (atoms)	5	7	13	27	66

Table 4.4: Critical Cluster Size Distribution

The comparative lack of oxygen precipitation defects in the opposite end, as compared to the seed end, specimens after 12+12 (industry and in-house) hours of annealing at 950°C indicates that thermal history in the puller was too short to create an appreciable number of clusters (e.g. >10^10/cc) above the critical (about 40 O-atom) size at 950°C, while thermal history for the seed end created ~10^11/cc of such clusters. The images of the seed-end specimen, figures 4.5 and 4.6, show these clusters after they had been grown to an easily detectable size in the TEM.

The specimens have a given oxygen number density near 10^{18} oxygen atoms per cubic centimeter. If prior nucleation history in the 600-800°C range created 10^{11} clusters/cc above the 950C critical size of around 40 O-atoms, then these could eventually grow to something as large as 10^{7} O-atoms in size, making them easily detectable in the TEM. [16]

A simple illustration of cluster abundance as a function of cluster-size uses Boltzmann-occupancy factors for the sub-critical distribution (assumed to rapidly reach steady-state). This shows growth by lateral transport of post-critical-sized

clusters up the cluster-size chain with help from oxygen's "direct-interstitial mechanism" diffusion-constant $D=DDe^{-\epsilon/kT}$ which should be relatively insensitive to other factors (like vacancy or impurity abundances). [17]

Figure 4.13 is a schematic of the Boltzmann probability-factors as a relative measure of the steady-state cluster number per unit-volume, versus cluster size. The blue line corresponds to hot silicon after solidification, whereas the orange line gives the "as-grown" distribution in a given part of the ingot after a gradual cool-down in the Cz puller. This ramped step was accomplished by lowering the temperature in 50^{o}C increments in the simulation. In both figures, a 1000^{o}C anneal was simulated after removal from the puller to facilitate the diffusion needed to precipitate most of the oxygen atoms in the wafer, assuming post-critical clusters are present. This is represented by the green line in the plot to the left, and the red line in the plot to the right. The plot to the right also reflects a short 800^{o}C pre-anneal before the 1000^{o}C precipitation run, represented by the green line. Vertical lines represent critical radius size for oxygen precipitate clusters.

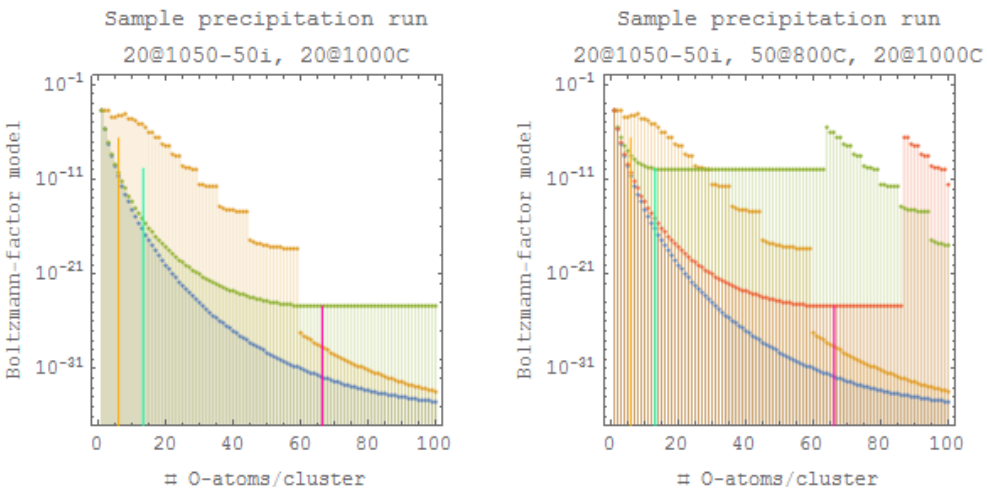

Figure 4.13: Boltzmann-factor cluster-distributions [35]

These schematic distributions evolve simply: Below critical radius tiny clusters either grow or evaporate quickly to the Boltzmann steady-state, while above critical radius and at the current temperature, the distribution simply shifts to the right as more oxygen is added to the clusters in existence. As you can see in figure 4.13, for example, the 1000°C treatment, in the absence of an 800°C growth step, has not found enough clusters above the critical size at 1000°C (refer to the appropriate vertical line) to result in a detectable number of growing precipitates.

Figure 4.13 also suggests that as-grown silicon is sure to contain a respectable number of clusters in the very-small size regime. Therefore, heat treatments, like the 800°C anneal in the plot to the right (followed by significantly more growth time during the 1000°C treatment) is the standard way in which that subcritical distribution can be characterized in the TEM or through etching. It also shows how precipitates can be created for use in the device manufacturing process itself.

Once again, to be quantitative in finding the number of grown precipitates, or developed oxygen clusters, per unit volume, quantitative ways to measure specimen thickness are needed.

Notable from figure 4.13, the pre-critical nuclei (or "latent clusters") should be observable, as their abundance is at least as great. The problem, however, is that these clusters may be un-strained, with neither strain-fields nor a Z-contrast advantage for the observer. This means that searches of only very thin regions with minimal surface "noise" will show promise. Hence the quest for specimen-preparation strategies, and instruments able to locate and characterize such tiny cluster-distributions in important materials, continues.

Figure 4.14 is a comparison of Boltzmann-factor precipitation cluster distribution taken one step further. Three single anneals after two different simple puller histories are shown. Figures (a), (b), and (c) are with a ramped cool down to mimic puller thermal history of seed end specimens, while (d), (e), (f) mimic the opposite end puller history. Each puller history is then correlated with a single anneal at 900^{o}C (figures a and d), 950^{o}C (figures b and e) and 1000^{o}C (figures c and f). The colored vertical lines again represent critical-sizes of clusters at the given temperature. The function lines represent cluster distributions: blue is the as-solidified 1050^{o}C, orange is the as-grown distribution (after cool-down in the puller), and green is the post-growth heat-treatment distribution. Here, clusters above the critical radius will grow with subsequent heat treatments, while any

below the critical radius will evaporate. In either case, the seed end of the ingot has a slower cool-down rate than the opposite end, hence resulting in differing critical size cluster distributions and ensuing cluster growth/evaporation. Note the as-grown distributions are stepped due to the incremental temperature drops during cooling time, slower at the seed-end than at the opposite end. Since the seed end of the ingot has a slower cool-down rate than the opposite end, it results in differing critical size cluster distributions and growth/evaporation. The graphs make it easily notable that differences in the puller history erase detectable differences at high temperatures (1000°C), whereas low temperatures (900°C) differences can only be preserved if one manages to retain and grow the flatter small-size part of the as-grown distribution curve.

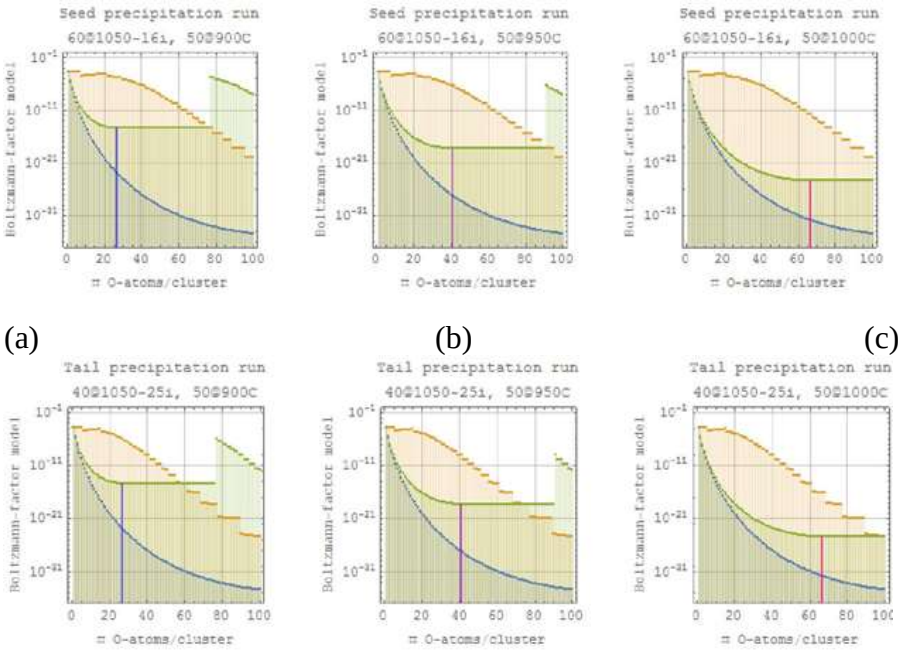

Figure 4.14: Cluster distributions for (a) seed-end puller history and 900°C anneal, (b) seed-end puller history and 950°C anneal, (c) seed-end puller history and 1000°C anneal, (d) opposite end puller history and 900°C anneal, (e)

5 Summary, Conclusions and Future Work

This project has contributed to advancements in specimen preparation and characterizations. In chapter 2, the challenges of isolating thin film GaSb devices was examined, as previous studies considered ELO an unfavorable method for these types of structures due to the lack of highly selective etchants. [5] The solution found in this project is to grow the GaSb devices on a GaAs substrate, and then use the typical ELO methods described in the literature. The addition of a GaAs and a copper protective layer further improved the surface of the thin films and thus optimize device efficiency. Further work on this part of the project could be useful in continuing to optimize the ELO process for GaSb films and investigating the resulting surface composition. Also, additional data from GaSb thin films fabricated into diodes would supplement the results.

For thickness characterizations, work on RGB analysis and stacking faults were expanded in chapter 3, allowing thickness measurements on areas without thickness fringes. As the RGB method is improved with future work, it may prove to be a useful method for a range of scientists. The most obvious application would be in the specialized semiconductor industry. As this is a silicon based method, it could be useful in electron microscopy of semiconductor devices. However, as this method is examined more closely and expanded beyond silicon, it could develop into an indispensable tool. Most cell phone cameras can get simple pictures that could serve as more than just beautiful images; These pictures can be analyzed for their red to green to blue ratios and give valuable data. For example, by measuring

the green component of images of two YBaCuO superconductors, the more completely oxidized batch might be identified when the eye alone could not have given this information. RGB ratios could also potentially be used to advise doctors on the level of oxygen or sugar in a patient's blood from the color differences that can be analyzed through RGB imaging. Moreover, as cell phone cameras are a cheap and readily available tool around the world, this method can be a quick and effective way to obtain preliminary data away from more specialized equipment. Thus, the study and development of this method will be a valuable asset to science.

A second short term future project for thickness measurements involves relating defect counts in the TEM to per-volume number densities. Because stacking faults offer a simple geometric measure of specimen thickness but are not generally present in modern silicon without both high oxygen content and long precipitation growth heat treatments, future work on specimens, with stacking faults already in hand, could facilitate a more quantitative calibration of the RGB thickness-measuring protocol in the lab. For defects in thin silicon, this technique provides a rapidly available map of thickness across a whole perforation, although a demonstrated protocol for its systematic use has yet to be ascertained.

Oxygen related defects in silicon were characterized in chapter 4 through a Boltzmann distribution factor pertaining to the thermal history of the specimen. For future work, establishing that the oxygen-precipitate precursor-phase nucleation increases minority-carrier lifetime in these specimens would be welcome, so that

both decreasing puller time in the 600-800°C temperature range or implementing a post-growth "high-temperature cluster-evaporation anneal" might be employed to improve minority-carrier lifetime. Cluster distribution models should be advanced to more comprehensive and accurate temperature versus time profiles. In addition, further experimentation may help confirm this possibility, as well as to see if methods to reduce precursor-phase abundance can increase minority-carrier lifetimes. A brief 800°C anneal might bring the opposite end material more into line with the seed end. Then, the abundance of as-grown clusters would be lessened by more rapid cooling (or a faster pull rate). Further annealing experiments could pre-emptively check to confirm or deny that such oxygen clusters are associated with a decrease in minority-carrier lifetime.

Acknowledgements

Foremost, I wish to acknowledge and thank Dr. Phil Fraundorf for support and guidance on this project and the energy he put in to being my research advisor and thesis committee chair.

Besides my chair, I would like to thank the rest of my thesis committee: Dr. David Osborn and Dr. Bernard Feldman.

I would also like to acknowledge and thank Dr. David Osborn and the Center for Nanoscience and Nanotechnology for support.

Thanks to the University of Missouri, Saint Louis, Department of Physics and Astronomy and the Missouri Space Grant Consortium for this project's financial support.

Special appreciation goes to Jai Kasthuri and Sun Edison Solar for providing funding and materials.

Thank you to Dr. Ganesh Balakrishnan and Emma Rentaria at the University of New Mexico and the Center for High Technology Materials for their support.

Special acknowledgements to: Stephen Ordway for the use of some of his prepared specimen and his helpful specimen preparation tutorials and advice, and Dr. Bernard Feldman for the use of the Advanced Physics Laboratory

Finally I want to thank everybody from the University of Missouri, Saint Louis Department of Astronomy and Physics for the exciting discussions and interesting suggestions throughout the duration of my enrollment as an MS student.

List of Figures

List of Tables

References

1. Fraundorf, P. "Roles for A Precursor Oxide Phase in The Siting, Shaping, and Shrinking of Oxygen Precipitates". (1985) MRS Proceedings, 59, 281 doi:10.1557/PROC-59-281.
2. Mack, Iris, Fraundorf, P. Spontaneously forming 30-150Å Defects at the Si/oxide interface. UM-STL Physics & Astronomy (17 July 2000)
3. Zhidan Zeng, Xiangyang Ma, Jiahe Chen, Deren Yang, Ingmar Ratschinski, Frank Hevroth, Hartmut S. Leipner . (2010). Effect of oxygen precipitates on dislocation motion in Czochralski silicon Journal of Crystal Growth, Volume 312, Issue 2, 1 January 2010, Pages 169-173.
4. J.P. McCaffrey, B.T. Sullivan, J.W. Frase, D.L. Callahan (1996) Use of transmitted color to calibrate the thickness of silicon samples. Micron, 27, 407-411
5. E. Renteria, P. Ahirwar, S. Clark, et al, “Isolation and Characterization of Large-Area GaSB Membranes Grown on GaAs Substrates,” Center for High Technology Materials, University of New Mexico, Albuquerque, NM, 87106, USA.
6. M. Konagai, M. Sugimoto, and K. Takahashi. "High efficiency GaAs thin film solar cells by peeled film technology." J. Cryst. Growth. 45, 277 (1978).
7. E. Yablonovitch, T. Gmitter, J. P. Harbison, and R. Bhat. "Extreme selectivity in the lift-off of epitaxial GaAs films." Appl. Phys. Lett. 51, 2222 (1987).

8. J. J Schermer, P. Mulder, G. J. Bauhuis, M. M. A. J. Voncken, J. Van Deelen, E. Haverkamp, and P. K. Larsen. "Epitaxial Lift-Off for large area thin film III/V devices." phys. Stat. soli. 202, 501 (2005).
9. S. H. Huang, G. Balakrishnan, A. Khoshakhlagh, A. Jallipalli, L. R. Dawson, and D. L. Huffaker, “Strain relief by periodic misfit arrays for low defect density GaSb on GaAs.” Appl. Phys. Lett. 88, 131911 (2006).
10. P. Y. Delaunay, B. M. Nguyen, D. Hofman, and M. Razeghi, “ Substrate removal for high quantum efficiency back side illuminated type-II InAs/GaSb photodetectors.” Appl. Phys. Lett. 91, 231106 (2007).
11. DeSalvo, R Kaspi, and C.A Bozada, “Citric Acid Etching of GaAsl_flbx, AIo.sGa0.sSb, and InAs far Heterostructure Device Fabrication.”J. Electrochem. Soc. 141 , 3526 (1994).
12. P. Hirsch, A. Howie, R. Nicolson, D.W. Pashley and M.j. Whelan (1965/1977) Electron microscopy of thin crystals (Butterworths/Krieger, London/Malabar FL) ISBN 0-88275-376-2
13. H. Siriwardane and P. Fraundorf (1994) "Quantitative footprints, in size & number density, of a TEM search for defects in VLSI silicon", Proc. Ann. Meeting - Electron Microscope
14. G. Fraundorf, P. Fraundorf, R. A. Craven, R. A. Frederick, J. W. Moody and R. W. Shaw (July 1985) "The effects of thermal history during growth on O-precipitation in Czochralski silicon", J. Electrochem. Soc. Solid State Science and Technology vol. 132 no. 7 pages 1701-1704.

15. R. Falster, V.V. Voronkov, V.Y. Resnik, M.G. Milvidskii. “Thresholds for effective internal gettering in silicon wafers,” Proceedings of the Electrochemical Society, VIII High Purity Silicon (2004), pp. 188–201

16. Fumio Shimura (1989) Semiconductor silicon crystal technology (Academic Press, San Diego CA).

17. Kelton, K.F. (1999). “Oxygen Precipitation in Silicon: Experimental studies and theoretical investigations within the classical theory of nucleation”. AIP Journal of Applied Physics 85, 8097 doi: 10.1063/11.370648.

18. J.D. Murphy, S. Senkader, R.J. Falster, P.R. Wilshaw . (2006). Oxygen transport in Czochralski silicon investigated by dislocation locking experiments Materials Science and Engineering: B, Volume 134, Issues 2–3, 15 October 2006, Pages 176-184

19. J.D. Murphy, S. Senkader, R.J. Falster, P.R. Wilshaw . (2006). Germanium-doped Czochralski silicon: Oxygen precipitates and their annealing behavior Materials Science in Semiconductor Processing, Volume 9, Issues 4–5, August–October 2006, Pages 600-605.

20. G. Fraundorf, P. Fraundorf, R. A. Craven, R. A. Frederick, J. W. Moody and R. W. Shaw. (1985). The effects of thermal history during growth on O-precipitation in Czochralski silicon. J. Electrochem. Soc. Solid State Science and Technology vol. 132 no. 7 pages 1701-1704.

21. P. Fraundorf, G. K. Fraundorf and F Shimura. (1985). The clustering of oxygen atoms around carbon in silicon. J. Appl. Phys. 58, 4049

22. J.D. Murphy, R.E. McGuire, K. Bothe, V.V. Voronkov, R.J. Falster. (2014). "Minority carrier lifetime in silicon photovoltaics: The effect of oxygen precipitation", Solar Energy Materials and Solar CellsVolume 120, Part A, Pages 402–411 abstract.

23. K. F. Kelton, R. Falster, D. Gambaro, M. Olmo, M. Cornara, and P. F. Wei. (1999). "Oxygen precipitation in silicon: Experimental studies and theoretical investigations within the classical theory of nucleation", J. Appl. Phys. 85:12, 8097-8111 (pdf)

24. A. Bourret, J. Thibault-Desseaux and D. N. Seidman. (1983). "Early stages of oxygen segregation and precipitation in silicon" J. Appl. Phys. 55:4, 825-836.

25. J.P. McCaffrey, B.T. Sullivan, J.W. Frase, D.L. Callahan (1996) “Use of transmitted color to calibrate the thickness of silicon samples,” Micron, 27, 407-411

26. Bracht, H. (2000). Diffusion mechanisms and intrinsic point-defect properties in silicon. MRS Bulletin, 22-27.

27. J. P. McCaffrey and J. Hulse (1998) Micron 29, Issues 2–3, Pages 139–144.

28. Fraundorf, P., Fraundorf, G. K. and Craven, R. A. (1985) "The induction effect for oxygen-precipitate nucleation in silicon: Evidence of a precursor", VLSI Science and Technology/1985, Proceedings Volume 85-5, (Electrochemical Society, Pennington NJ) 436-445.

29. Ham, Frank. (1958). “Theory of Diffusion-Limited Precipitation”. Phys. Chem. Solids, Vol. 6, 335-351.

30. Kelton, K.F. (2003). “Diffusion-influenced nucleation: a case study of oxygen precipitation in silicon”. Phil. Trans. R. Soc. Lond. A 361, 429-446.

31. Fumio Shimura (1989) Semiconductor silicon crystal technology (Academic Press, San Diego CA).

32. J. P. McCaffrey and J. Hulse (1998) Micron 29, Issues 2–3, Pages 139–144.

33. Roberts, J, Fraundorf, F. (2014). RGB analysis of wedge angles around a perforation in silicon. Microscopy and Microanalysis Conference proceedings, 7 August 2014.

34. Zhidan Zeng, Jiahe Chen, Yuheng Zeng, Xiangyang Ma, Deren Yang. (2011). Immobilization of dislocations by oxygen precipitates in Czochralski silicon: Feasibility of precipitation strengthening mechanism Journal of Crystal Growth, Volume 324, Issue 1, 1 June 2011, Pages 93-97.

35. Roberts, Jamie, Fraundorf, P., Kasthuri, Jai and Osborn, David. (2016) "Exploring Boltzmann-Factor Distributions of Precipitation-Nuclei in the TEM",Microscopy and Microanalysis 22:S3, 942-943